Helmholtz-Zentrum Dresden-Rossendorf (HZDR)

HZDR
HELMHOLTZ ZENTRUM
DRESDEN ROSSENDORF

Defect-induced magnetism in SiC

Zhou, S.; Chen, X.;

Originally published:

July 2019

Journal of Physics D: Applied Physics 52(2019), 393001

DOI: https://doi.org/10.1088/1361-6463/ab2495

Perma-Link to Publication Repository of HZDR:

https://www.hzdr.de/publications/Publ-29485

Release of the secondary publication
on the basis of the German Copyright Law § 38 Section 4.

Defect induced magnetism in SiC

Shengqiang Zhou

Helmholtz-Zentrum Dresden-Rossendorf, Institute of Ion Beam Physics and Materials Research, Bautzner Landstrasse 400, D-01328 Dresden, Germany

E-mail: `s.zhou@hzdr.de`

Xiaolong Chen

Research & Development Center for Functional Crystals, Laboratory of Advanced Materials & Electron Microscopy, Beijing National Laboratory for Condensed Matter Physics, Institute of Physics, Chinese Academy of Sciences, Beijing 100190
University of Chinese Academy of Sciences, Beijing 100049
Collaborative Innovation Center of Quantum Matter, Beijing 100084

E-mail: `chenx29@iphy.ac.cn`

Abstract. Defect induced magnetism describes a magnetic phenomenon in materials containing neither unpaired $3d$ nor $4f$ electrons. Therefore, it presents a challenge to the conventional understanding of magnetism and has remained under debate over a decade. Different from graphite and oxides which are common research venues of defect-induced magnetism, SiC is commercially available at large scale and with high quality at the microelectronic grade. Therefore, SiC presents a suitable model system for studying defect-induced ferromagnetism and exploring possible applications. Understanding and controlling defect-induced magnetism in a semiconductor like SiC opens up the possibility for producing spintronic devices based on classical semiconductor technologies. Here, we review recent studies on defect induced magnetism in SiC. We start with a brief description about defects in SiC. Then we summarize the experimental results on defect induced magnetism in SiC, the microscopic origin of the magnetism and the magnetic coupling mechanism. We also propose several potential applications, particularly using magnetometry as a complementary method for quantitative characterization of defects in SiC. At the end, we list the challenges from our point of view, such as controlling defects in SiC regarding their charge states, distribution and local environment, and understanding defect-induced magnetism by local and elemental selective probe techniques.

PACS numbers: 75.50.Pp, 78.70.-g

Keywords: SiC, Magnetism, Defects

Submitted to: *J. Phys. D: Appl. Phys.*

1. Introduction

Over the last decade, the study of dilute magnetic semiconductors has undergone a transition from doping $3d$ elements to creating defects in the host semiconductor. This is, in particular, true for SiC. On one hand, since SiC has a very rigid lattice, the solid solubility of $3d$ elements is very limited. The observed ferromagnetism at varying temperatures is often in debate. The focus of the debate lies in whether the magnetism really comes from the intrinsic doped SiC or from other sources, such as resultant secondary phases or $3d$ metal precipitates. These secondary phases and precipitates, though in a tiny amount, often can be responsible for the observed magnetism. For instance, it has been demonstrated that the main source of the magnetism in Fe implanted SiC is due to the secondary phase Fe_3Si by using the atomic probe tomography and ^{57}Fe Mössbauer spectroscopy [1, 2].

On the other hand, it is well known that localized magnetic moments and the coupling between them are two indispensable factors to induce long-range spin ordering in solids, such as ferromagnetism (FM), antiferromagnetism (AFM), ferrimagnetism, etc. Previously, only atoms that contain the partially filled $3d$ or $4f$ subshells are thought to produce local moments according to the Hund's rule. Spontaneous spin coupling tends to occur and leads to various long-range orderings depending on the nearest- and next-nearest spin-spin exchange integrals. In general, the coupling strength is sensitive to the separation of the spins. Coupling over a large separation is possible if the wave functions have sufficient spatial extent. This is the case for dilute magnetic semiconductors, where the concentrations of $3d$ metals are in a range from less than one to a few atomic percent and the free carriers mediate the magnetic coupling [3]. Recent progresses, however, have been accumulating evidence that intrinsic magnetism can come from some kinds of defects in a variety of solids. For instance, room temperature ferromagnetism was observed in highly oriented pyrolytic graphite (HOPG)[4, 5, 6], in HfO_2 [7], in Al doped SiC [8], in Li-doped ZnO [9], and in various nano-sized compounds [10, 11] that are otherwise nonmagnetic in their bulk states. See Refs. [12, 13, 14] for recent reviews.

Different from graphite and oxides which are common research venues of defect-induced magnetism, SiC is commercially available at large scale and with high quality at the microelectronic grade. Therefore, SiC presents a suitable model system for studying defect-induced ferromagnetism and for exploring possible applications. Here, we review recent studies on defect induced magnetism in SiC. We also propose the potential applications and list the challenges to control the defect-induced magnetism in SiC from our point of view.

2. Introducing defects in SiC

SiC is a wide bandgap semiconductor, belonging to the class of 3rd generation semiconductors. Due to its outstanding properties such as high thermal conductivity, high breakdown voltage and high saturated electron drift velocity, SiC is steadily

Table 1. Spin values for the stable charge states of the N_CV_{Si}, V_{Si}, and V_C defects in 4H-SiC. From Ref. [20]

Charge state	N_CV_{Si}	V_{Si}	V_C
+2	unstable	unstable	0
+1	unstable	unstable	1/2
0	1/2	1	0
-1	1	3/2	3/2
-2	1/2	1	0

replacing conventional semiconductor materials, e.g., silicon (Si) and gallium arsenide (GaAs) for certain extreme applications [15]. Therefore, to understand and control the defects is interesting in general. When talking about defects in SiC, one has to note its large number of polytypes [16]. Up to now, more than 200 types of phases of SiC have been found. The technically interesting polytypes are 4H-, 6H- and 3C-SiC. Both 4H- and 6H-SiC are hexagonal and have bandgaps of 3.26 and 3.02 eV, respectively [17]. 3C-SiC is cubic and also called β-SiC with a bandgap of 2.4 eV [17].

High-purity SiC (doping less than 10^{16} cm^{-3}) has been grown by high temperature chemical vapour deposition (HTCVD), physical vapour transport (PVT) and chemical vapour deposition (CVD). Extended defects in SiC include 1) open-core dislocations (also known as micropipes), 2) low-angle boundaries and 3) conventional dislocations [18]. However, those extended defects are not within the scope of this review, although they may play an important role in the magnetic coupling. In the current review, we focus on the point defects, like vacancies, interstitials, anti-sites and their complexes [19]. Those point defects can have spin and therefore act as local moments. As an example, Weber *et al.* [20] have calculated the spin values for different defects in 4H-SiC, as listed in Table 2.

2.1. By changing growth condition

Bechstedt *et al.* have studied the prototypical native defects, in particular monovacancies, in 3C- and 4H-SiC by using *ab initio* density functional theory and the local spin-density approximation [21]. Carbon vacancies with 2+ charge have the lowest formation energies (hence, highest defect concentrations) under p-type doping and both Si-rich and C-rich preparation conditions. Carbon vacancies are double donors and dramatically reduce the doping efficiency of acceptors.

Therefore, electrically active defects in SiC depend strongly on the growth conditions. Experimentally, the main knobs are the growth temperature, the growth pressure and the C/Si pressure ratio. Kimoto *et al.* have grown 4H-SiC by a horizontal hot-wall CVD system under different reactor pressure and different C/Si ratio [22]. The electron concentration (for unintentionally doped samples) increases with increasing the reactor pressure. The total trap concentration is also reduced by increasing the input C/Si ratio. Another work from the same group again confirms that C-rich condition is

favorable to reduce intrinsic defects [23].

Zhang *et al.* have investigated the electrically active defects in the epilayers grown with fast epitaxy by a vertical, hot-wall CVD reactor [24]. They found intrinsic defects and impurities such as B and Ti in most of the epilayers. The intrinsic defect concentration increases with the growth temperature. The incorporation of shallow B impurities is enhanced at lower temperatures and can be increased by increasing the C/Si ratio. The Ti concentration does not show a clear temperature dependence, but increases with increasing the C/Si ratio. The concentrations of EH6/7 (electron traps) and HS1 (hole traps) are reduced at higher C/Si ratio, and the $Z_{1/2}$ (electron traps) concentration is not sensitive to the C/Si ratio [24].

2.2. By ion irradiation

Taking the advancing of accelerator technologies, a variety of ions (all stable elements and some radioactive elements) in a wide energy range from eV to hundreds of GeV can be produced and injected into targets. Using the chemical effect of injected ions, the technique "ion implantation" is a common technique to dope semiconductors. This technique has been integrated into the standard microelectronics production line for integrated circuits in silicon technology. Ion irradiation refers to using other effects rather than the doping effect in materials. Compared with varying growth and/or annealing parameters to control defects in SiC, the use of an ion beam has a number of advantages:

- High speed and reproducibility;
- Exact control of the implantation fluence by integration of the beam current;
- Exact control of the implantation energy to generate defects in different depth;
- Simple masking methods to make lateral patterns for devices.

The ions implanted into a semiconductor undergo collisions with the target atoms, and lose their energies due to the ion stopping process. The total energy loss per unit distance is determined by the electronic stopping and the nuclear stopping. In the former process, the ion energy is lost by excitation and ionization of atoms (inelastic). The lost energy eventually dissipates as heat, and does not create atomic displacements in the materials. The electronic stopping cross section is proportional to the velocity of the ions. Its contribution dominates in the high-energy regime. Nuclear stopping occurs as a result of elastic collisions of ions with nuclei in the target, and leads to atomic displacements. These displaced atoms may have enough energy to displace others, resulting in a cascade of recoiled atoms. Nuclear energy loss dominates at intermediate energies (hundreds of keV), and leads to the creation of deep-level compensating defects. At high energies, the contribution from nuclear stopping tends to be small because fast ions have only a short time to interact with a target nucleus, and cannot transfer energy efficiently. Figure 1 shows a schematic of the relative energy loss due to electronic and nuclear stopping processes as a function of ion energy.

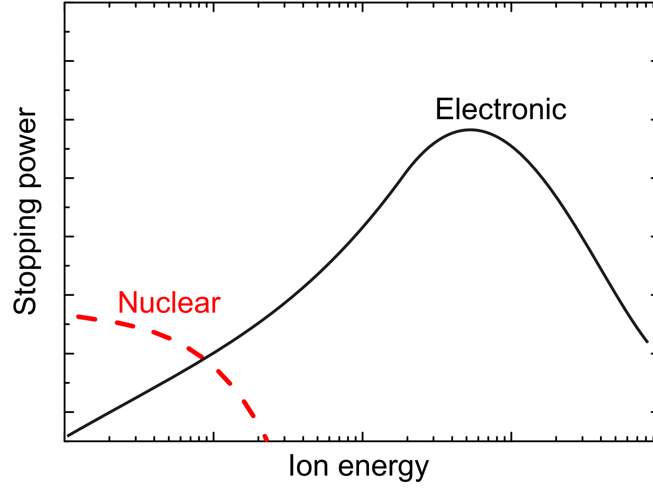

Figure 1. Schematic of the cross section for electronic and nuclear stopping processes as a function of ion energy [25].

One of the most important parameters that determine the extent of lattice damage is the threshold displacement energy, E_d. This is defined as the minimum kinetic energy to be transferred to an atom to displace it from its lattice site, resulting in a stable Frenkel pair. Devanathan and Weber used molecular dynamics simulations to calculate E_d in 3C- and 6H-SiC [26]. The two polytypes show many similarities in the nature of the E_d surface. The minimum displacement energies are 21 eV for C and 35 eV for Si in both 3C-SiC and 6H-SiC, and the values are in good agreement with interpretation of experimental observations. One of the drawback of using ion beams to create defects is the lack of selectivity for producing specific defects. Particularly, in compound semiconductors ion irradiation always produces many kinds of defects, such as vacancies and interstitials of each constituent element as well as antisites.

SRIM (the Stopping and Range of Ions in Matter) is the most comprehensive program available to calculate the interactions between ions and matter. This is a Monte Carlo program developed by J.F. Ziegler and J.P. Biersack [25], which will calculate both the total three dimensional distribution of the ions and also all kinetic phenomena associated with the ion's energy loss: target damage, sputtering, ionization, and phonon production. An example is given in Figure 2 for hydrogen and neon ion implanted 6H-SiC. The distributions of the radiation damages have been estimated from Monte Carlo calculations using SRIM2003 with a density of 3.21 g/cm^3 and displacement energy of 21 eV for C and 35 eV for Si. The *dpa* (displacement per atom) is calculated as: $dpa =$ implantation fluence $\times$ displacements per ion and unit depth / atomic density, where the displacements are calculated by the SRIM code. By varying the ion energy, one can place the defect in different depth. Heavier ions (here Ne) produce much more defects

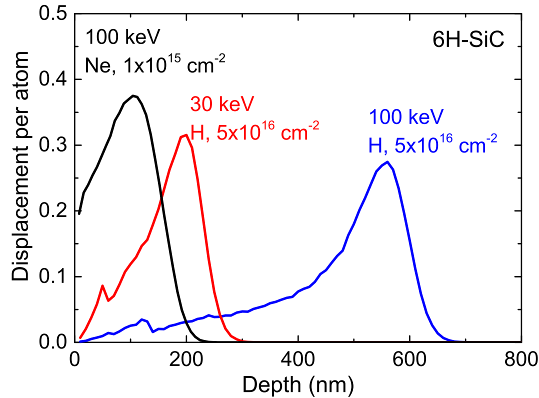

Figure 2. SRIM simulation of displacements per atom (dpa, solid lines) in 6H-SiC for 30 keV and 100 keV H ion implantation at the fluence of 5×10^{16} cm^{-2}, and for 100 keV Ne ion implantation at the fluence of 1×10^{15} cm^{-2}. The heavier ions at lower energy produce much more defects than light ions.

than light ions. Note that the SRIM code does not take into account the recombination of the primary interstitials and vacancies and thus the actual damage levels in the sample can be lower than the simulated values.

2.3. By electron irradiation

Energetic electrons interact with the nuclei and the electron system in the target. Because of momentum conservation, only a small fraction of the impinging electron energy can be transferred to a nucleus. Comparing with ions, a rather high electron energy ("threshold energy") is needed to displace an atom. The energy is transferred via electron-nucleus scattering. For example, an electron energy of 100 keV is needed to transfer around 20 eV to a carbon atom. This is close to the threshold for moving the carbon atom in the graphitic structure [27]. Note that displacement energies in SiC are 21 eV and 35 eV for C and Si, respectively. On the other hand, electron-electron scattering already occurs at low electron energies and may cause ionization or bond breaking. Normally, this kind of energy transfer does not result in atom displacements but may introduce defects in the target due to beam-stimulated local chemical reactions. The cross sections of both nuclear and electron scattering decrease with increasing electron energy.

It is interesting to note that for SiC, the Si/C mass ratio is around 2.33, resulting in clearly separated irradiation energy thresholds for the displacements of different lattice atoms. It has been suggested that the threshold energies of an electron to displace C and Si in SiC are 100 and 250 keV, respectively [28]. Therefore, with low energy electron irradiation in the 100 – 250 keV range, one can create only those intrinsic defects related to the initial displacements of carbon atoms in the SiC [29].

2.4. By neutron irradiation

Neutrons are uncharged particles. Therefore, neutrons have no interaction with atomic electrons, but only interact with nuclei in the material. The nuclear force, leading to the interaction between neutrons and nucleus, is very short ranged. Given the fact that the size of the nucleus in relation to the atom is very small, neutrons have low probability of interaction and can penetrate very large distance before being slowed down. The process of creating crystal lattice damages during neutron irradiation is due to the scattering of the energetic neutrons by the nuclei of the target atoms. The neutrons are generally produced by nuclear fission and their energies extend over a wide range of energy from meV to around 10 MeV, with a mean energy of 2 MeV. The displacement energy thresholds of C and Si in SiC are in the order of 20 and 30 eV, respectively. It is reasonable to assume that the transferred energy from the neutron to the nucleus which will irreversibly displace the lattice atoms from its site will be a few times the displace threshold. Neutrons with energies larger than about 100 eV (including epithermal neutrons with energy 50 eV – 500 keV and fast neutrons with energy 50 keV – 10 MeV [30]) can produce displacements and the displaced atoms with greater energies produce further displacements in collisions with other target atoms in a cascade. The elastic scattering dominates when the energy is below 5.5 MeV in carbon and the nuclear reaction (inelastic scattering) only becomes significant when the energy is above 9 MeV [31].

As an example, at the chamber DBVK at the BER II reactor at Helmholtz–Zentrum Berlin, the fluxes are 1.08×10^{14} $cm^{-2}s^{-1}$ of thermal neutrons below 50 eV, 7.04×10^{12} $cm^{-2}s^{-1}$ of epithermal neutrons, and 5.80×10^{13} $cm^{-2}s^{-1}$ of fast neutrons, respectively. Comparing with epithermal or fast neutrons, thermal neutrons only produce negligible displacement. Therefore, only epithermal and fast neutrons are accounted for in the fluence calculation.

2.5. Comments on different irradiation methods

Ions are available at implanters and high energy electrons are produced by accelerators and low energy electrons are also available at scanning electron microscopy and transmission electron microscopy. Those facilities are generally accessible at many universities/research institutes. However, neutron sources are limited at nuclear reactors with limited availability and access. One also has to note that neutron also induces activation of heavy elements. After neutron irradiation, the samples have to be checked until they decay to a safe level before the structural, electrical and magnetic measurements can be performed.

On the other hand, the microscopic structure of most of the defects created by irradiation is poorly understood. This is not surprising, since the number of possible defect configurations created by high energy particles is huge and difficult to treat. In many cases it is not even known which atom - carbon or silicon or both - is involved in the formation of the defect center. Electron irradiation gives the possibility to selectively

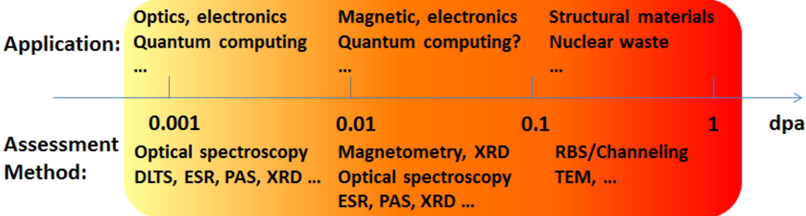

Figure 3. Schematic representation of the investigation of defects in irradiated SiC concerning applications and assessment methods. DLTS: deep-level transient spectroscopy; ESR: electron spin resonance; PAS: Positron annihilation spectroscopy; XRD: x-ray diffraction; RBS/Channeling: Rutherford backscattering/channeling; TEM: transmission electron microscopy.

induce defects in SiC since the displacement threshold energy to move Si or C is much different.

We also should know the collision cross-section of different irradiation sources with SiC, in another word, the possibility of inducing defects. As a thumb rule, ions have the largest possibility due to their large mass in comparison with electron. Neutrons have the smallest cross-section since only strong interaction is involved. As an example, the cross-section of MeV neutrons is smaller than MeV Ar ions by around 4 orders of magnitude [32].

2.6. Identify defects

To measure defects in SiC, different methods have been well developed for samples with different defect concentrations. For irradiation induced defects, a useful parameter to quantify the amount of defects is the displacement of lattice atom (*dpa*). The *dpa* is calculated as: dpa = implantation fluence $\times$ displacements per ion and unit depth / atomic density, where the displacements can be calculated by the SRIM code [25].

In figure 3, we schematically compare different measurement techniques regarding the applicable defect concentration. Rutherford backscattering/channeling is generally sensitive to point defects at relatively high concentration, but is difficult to identify the nature of the defects, *i.e.* single vacancy, double vacancy. Transmission electron microscopy is powerful in detecting extended defects, however it is difficult to find point defects at low concentrations. Electron paramagnetic resonance [33, 34] and optically detected magnetic resonance [35] are sensitive in identifying point defects in SiC. Hyperfine interaction due to ^{29}Si and ^{13}C is decisive information, which can be used to extract not only the chemical identity but also the local geometry and the electronic state of defects.

Photoluminescence, particularly the zero-phonon line (ZPL), is also fingerprint of different point defects. For instance, in 4H-SiC ZPL was calculated for different divacancy: the *kk* and *hh* forms of the axial divacancy (*k* stands for quasicubic position and *h* for quasihexagonal), and the *kh* and *hk* forms of the basal divacancy. The energies

of ZPL can be used to distinguish the four forms of divacancy [36]. The calculation is in well agreement with experimental results [37].

Deep-level transient spectroscopy (DLTS) is a suitable technique to investigate electrically active point defects in SiC [38, 39, 40]. The defects reflect themselves as DLTS peaks in the spectrum as a function of temperature. Carbon vacancies have been clarified to be the major electrically active defects in 4H-SiC and they are serious obstacles for high-voltage bipolar devices [41].

For the above-mentioned methods, we recommend different review or research articles cited in this manuscript. We will introduce a little more on positron annihilation spectroscopy (PAS) [42]. PAS has been used as a nondestructive probe in semiconductors because of its high sensitivity to neutral or negatively charged vacancies and vacancy-clusters. Vacancies in the semiconductor can trap implanted positrons into localized states which have a longer positron lifetime compared to delocalized positrons, since the electron density at the vacancy site is lower. Different vacancies can be identified by their characteristic positron lifetimes, which are fingerprints of the corresponding defects.

Figure 4 shows typical positron lifetime spectra in electron irradiated SiC [43]. In this measurement, the lifetimes of a huge amount of positrons are recorded by detecting the birth of the positron and the subsequent radiation emitted by annihilation. In another word, the lifetime is the delay between the position emission and annihilation. Positrons annihilate at different lattice sites. Each of them has a characteristic lifetime. Since annihilation is a statistical process, many annihilation events have to be recorded and are placed in a histogram in order to determine the positron lifetime in the measured specimen. The intensity (or counts) represents the annihilation events at a particular time. It is often given in a relative manner. From Fig. 4, one can see the lifetime increases with the irradiation fluence. Generally, a multi-component fit was used to separate different contributions in the spectra. In these two particular spectra shown in Fig. 4, two life components were obtained. One is the short component $\tau_1 \sim 159\,\mathrm{ps}$ which is very close to the free lifetime due to single vacancies. The second component $\tau_2 \sim 210\,\mathrm{ps}$ is due to divacancies. A similar lifetime $\tau_2 \sim 225\,\mathrm{ps}$ was also measured by Ling *et al.* and was attributed to divacancies in doped 6H-SiC [44, 45]. Brauer *et al.* investigated the positron lifetime in vacancy clusters in 3C-SiC and 6H-SiC [46]. The lifetime increases with the size of vacancy clusters. In ion implanted SiC, the positron lifetime also increases with increasing ion fluence, indicating the divacancy clustering and crystalline amorphisation [47].

In addition to identify the defect types, the multi-component fitting for the lifetime spectra also gives the intensity of each component. The intensity carries information of defect concentration. Figure 5 shows τ_2 and its intensity as a function of the positron energy. It also provides the depth distribution of the defects. By knowing the positron trapping rate of a particular defects, one can calculate the defect density through the procedure described in Ref. [47] and its depth profile. It was estimated that the divacancy concentration in the damaged layer (the top 300 nm) is 44 ppm in

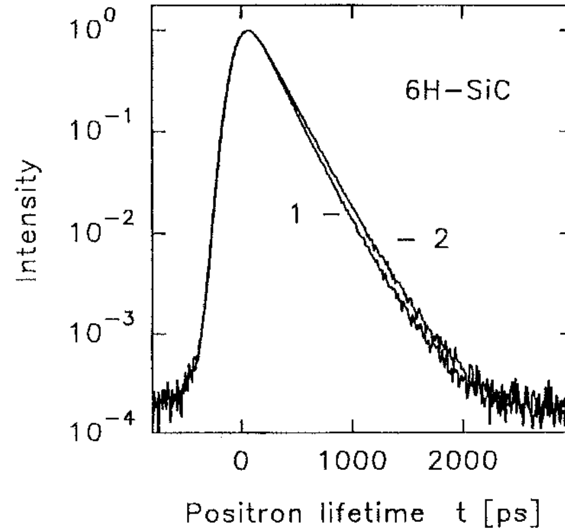

Figure 4. Positron lifetime spectra in low-temperature electron irradiated 6H-SiC with the following electron energies and irradiation fluences (ϕ): 1 - E = 2.5 MeV and ϕ = 1.3 × 10^{18} e/cm^2; 2 - E = 2.5 MeV and ϕ = 1.2 × 10^{19} e/cm^2. Figure is from Ref. [43].

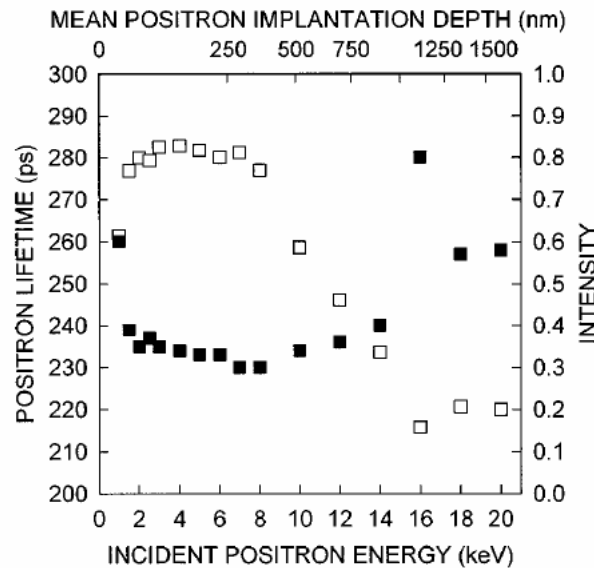

Figure 5. Second positron lifetime τ_2 (solid squares, left y axis) and its relative intensity I_2 (open squares, right y axis) as a function of incident positron energy E for 200 keV Ge implanted 6H-SiC with the fluence of 1 × 10^{17} cm^{-2}. The depth is estimated and shown as the top x axis. Figure is from Ref. [47].

this particular sample shown in Fig. 5. Indeed, the lifetime measurement was also done for neutron irradiated, ferromagnetic SiC [48], as shown later in Fig. 10.

Beside the lifetime, positron annihilation Doppler broadening spectroscopy (DBS) is also able to identify the defect type. When positrons annihilate with electrons, two 511 keV photons will emit. The Doppler broadening of the 511 keV gamma emission

peak is mainly caused by the momentum of the electron due to the very low momentum of the thermalized positron and is characterized by the line-shape parameter S [49]. The value of S is defined as the ratio of counts in the central region of the annihilation gamma peak to the total number of counts in the peak. The energy regions are selected to give S=0.5 for the virgin bulk material and then fixed for the irradiated samples. The S-parameter characterizes the positron annihilation with low momentum electrons and it increases with increasing size of the particular open volume defects (e.g., vacancy clusters). In Ref. [47], the authors have shown that V_{Si}-V_C divacancies in 6H-SiC can be identified by a S-parameter of 0.5375. In Ref. [49], the authors established a relationship between the number of clustered divacancies and the S-parameter.

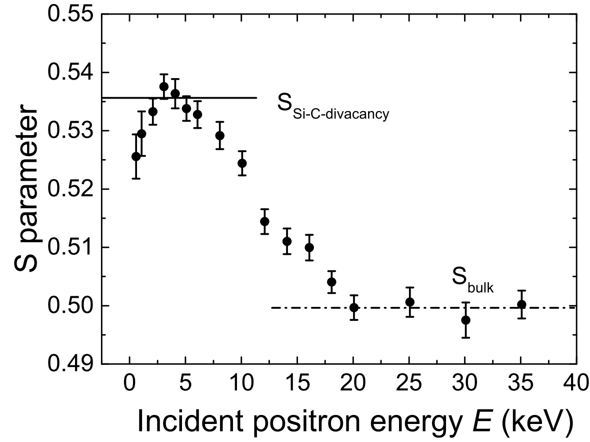

Figure 6. S parameter versus incident positron energy of the Xe implanted 6H-SiC sample at the energy of 500 keV and the fluence of 5×10^{12} cm^{-2}. Figure is from Ref. [50].

Figure 6 shows the measured S parameter versus the incident positron energy for 500 keV Xe irradiated 6H-SiC. The maximum of the S parameter around positron energy of 3–4 keV corresponds to positron annihilation in the defects created by ion implantation within a depth of about 200 nm. For higher positron energies the positron annihilation is shifted more and more to the undamaged bulk material, the S parameter decreases and finally reaches the bulk value at 20 keV (dash-dot line in Fig. 6). The S parameter of the V_{Si}-V_C divacancy is plotted as a solid line in Fig. 6. The S parameter of the defects in the Xe ion irradiated sample agrees well with that for the V_{Si}-V_C divacancy.

In this section, we have briefly discussed about different methods to characterize defects in SiC. However, one has to note that SiC is a binary compound semiconductor. The displaced atoms and implanted ions have many different possibilities to occupy substitutional-, interstitial- and anti-sites. This eventually results in many features in the measurement spectrum and gives difficulty to assign the features to the structural defects. Further, many unequivalent lattice sites also can lead to a broad, featureless

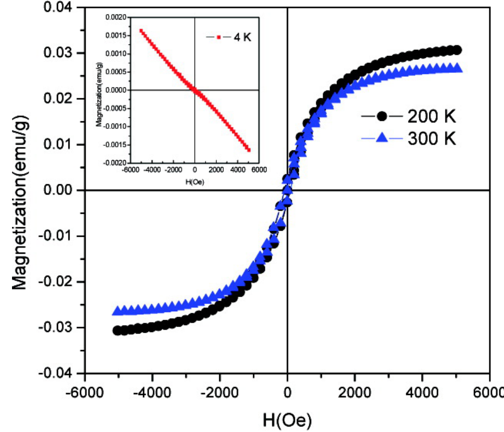

Figure 7. Hysteresis loops for Al-doped 4H-SiC, observed at 200 K (circles) and 300 K (triangles). The inset shows the hysteresis loops at T = 4 K (squares) for the undoped 4H-SiC obtained at the same experimental conditions. Figure is from Ref. [8].

spectrum. Therefore, to identify the structural defects first-principle calculations are often needed. Moreover, different experimental techniques should be used and the results should be compared.

3. Defect induced magnetism in SiC

3.1. Ferromagnetism

The first report about magnetism in SiC which is not doped with transition metal is about the glassy ferromagnetism in Al doped 4H-SiC as shown in Figure 7. In the work by Song *et al.* [8], magnetic hysteresis was observed for single phase Al-doped 4H-SiC at room temperature, but not observed for undoped samples down to 4 K. The sample was prepared by single crystal growth with Al concentration of $\sim$ 0.75 atom%. Zero-field-cooled (ZFC) and field-cooled (FC) temperature dependence of dc magnetization at different field was measured. At low field, a pronounced ZFC-FC irreversibility is revealed and the irreversibility becomes weaker with increasing the applied field. These features are the fingerprints for spin glass (SG) systems.

The authors proposed that the formation of local magnetic moment in Al-doped 4H-SiC is related to the conversion from carbon sp^3 to sp^2. Upon Al doping in SiC, some C-Si bonds (sp^3 configuration with a bond energy of 301 kJ·mol^{-1}) can be converted to C-Al bonds in sp^2 plane configuration. The trivalent Al ions substitute Si sites, leading to a mixture of sp^3/sp^2 hybridization. The unpaired electron is prompted to a higher orbital enabling it to participate in the magnetic ordering. To induce the ferromagnetic coupling, a strong enough correlation between these local spins must exist. The authors suggested that the structural defects induced by Al doping can serve as this mediation. Later, a study by means of first–principles calculations suggested that the complex of substitution Al for Si together with a Si vacancy can induce spin–polarization and local magnetic moment in Al-doped 4H-SiC [51]. The interaction between the local moments

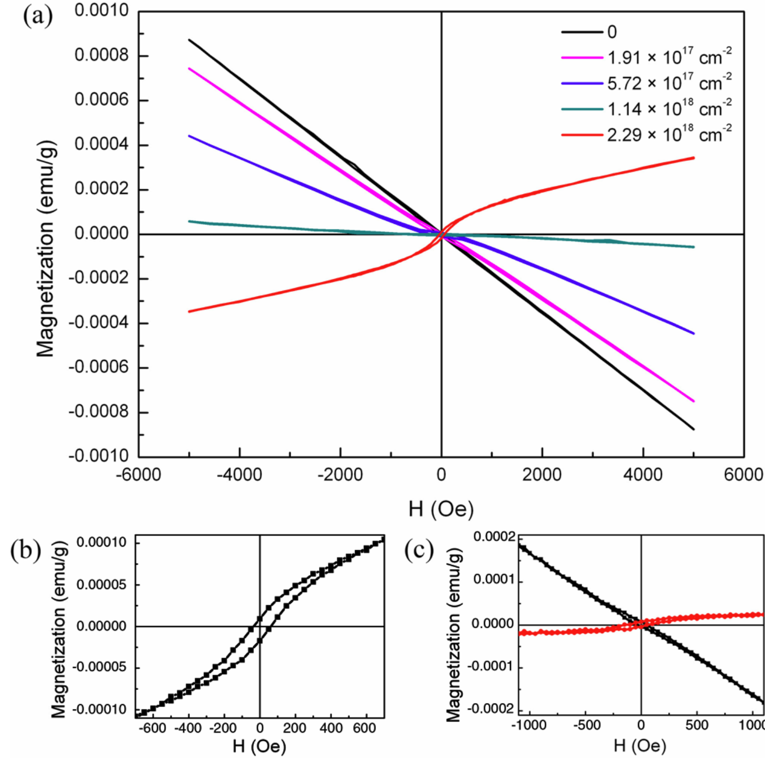

Figure 8. (a) The magnetization measured at T = 5 K as a function of magnetic field for neutron irradiated and pristine 6H-SiC samples. (b) The magnified hysteresis loop for the sample with the fluence of 2.29×10^{18} n/cm^2 at T = 5 K. (c) The magnetic signals with (black) and without (red) the diamagnetic contribution in the low-magnetic field range for the sample with fluence of 2.29×10^{18} n/cm^2 at T = 300 K. Figure is from Ref. [48].

results in the ferromagnetic order.

Liu *et al.* reported defect-induced magnetism in neutron irradiated 6H-SiC single crystals [48]. In this work, a correlation between structure and magnetism was given in details. The starting samples are commercially available 2 inch semi-insulating p-type 6H-SiC (0001) wafer. The neutron fluence was varied from 1.91×10^{17} n/cm^2 to 2.29×10^{18} n/cm^2. Figure 8 shows the magnetization with varied applied field at 5 K. In the pristine sample, only diamagnetic features have been observed. After a low fluence irradiation at 1.91×10^{17} n/cm^2, a weak hysteresis loop can be seen in the low-field range. With increasing irradiation fluence, the diamagnetism becomes weaker and the hysteresis loops arise. At a fluence of 2.29×10^{18} n/cm^2, a distinct hysteresis loop can be clearly observed as shown in Fig. 8(b). The saturation magnetization reaches 1×10^{-4} emu/g. Even at 300 K, the hysteresis loop can still be observed as shown in Fig. 8(c). It is suggested that the ferromagnetism is not homogeneously distributed but probably exists in domains. Therefore, the magnetization values obtained by dividing the magnetic moment by the total mass do not correspond to the expected intrinsic values.

The defective structure in those neutron irradiated 6H-SiC was investigated by

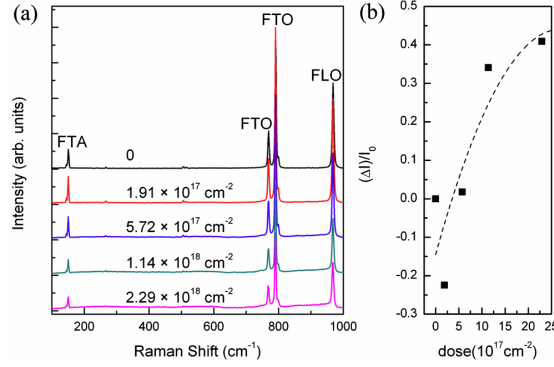

Figure 9. (a) Raman spectra from 100 cm^{-1} to 1000 $^{-1}$ for irradiated and pristine 6H-SiC samples. (b) The relative intensity of the folded longitudinal optical (FLO) mode versus the irradiation fluence. The dashed line is a guide to the eyes. Figure is from Ref. [48].

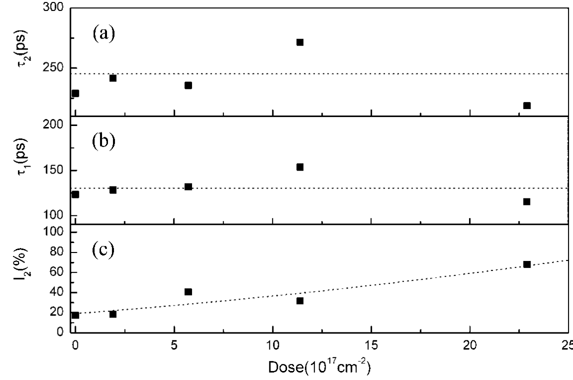

Figure 10. Fitted results of τ_2 (a), τ_1 (b) and I_2 (c) as functions of the irradiation fluence. Both τ_1 and τ_2 are found to be independent of fluence. I_2 is demonstrated to have positive correlation with the fluence. The dotted line shows the average values in (a) and (b). But the dotted line is only a guide to the relationship between I_2 and the irradiation fluence in (c). Figure is from Ref. [48].

Raman scattering, as shown in Fig. 9(a). The decrease in Raman intensity for each mode with increasing irradiation fluence is a direct reflection of the lattice damage. Figure 9(b) shows the relative intensity variation of the folded longitudinal optical (FLO) mode given by (1-I/I_0) vs. fluence, where I_0 and I are the intensities of the peak measured in the pristine and irradiated samples, respectively. Such a change in the relative intensity suggests the existence of defects in the irradiated samples.

To investigate the nature of defects created by neutron irradiation, positron annihilation lifetime spectroscopy (PALS) was performed. The lifetime spectrum is obtained and decomposed into lifetimes correlated with different annihilation sites. The fitted positron lifetimes τ_1, τ_2, and the fraction of the defects with longer lifetime (τ_2) I_2 as functions of the irradiation fluence are shown in Fig. 10. It is found that the lifetimes τ_1 around 130 ± 14 ps and τ_2 around 239 ± 20 ps are independent of irradiation fluence, and I_2 is proportional to the irradiation fluence within the fluence range applied

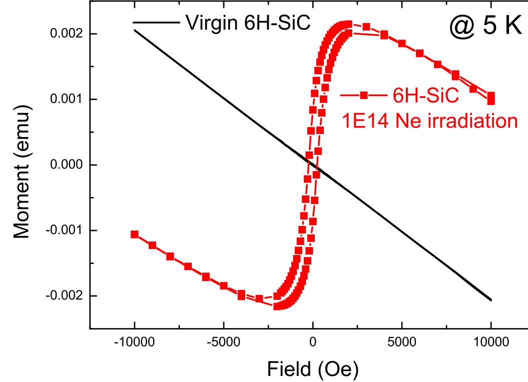

Figure 11. Magnetic properties of virgin and ion irradiated (1E14: ion fluence 1×10^{14} cm^{-2}) 6H-SiC measured at 5 K. Both samples were originally cut from the same wafer. The result has been published in ref. [53].

in this study. The lifetime value of 130±14 ps, can be assigned to the bulk lifetime of 6H-SiC. The positron trapping center at 239±20 ps, is close to 253±4 ps and 225±11 ps. It is suggested to be V_{Si}-V_C divacancy in 6H-SiC crystals. The dependence of I_2 on irradiation fluence suggests that the concentration of V_{Si}-V_C increases with the fluence.

Therefore, considering the full picture shown in Ref. [48], it is reasonable to correlate the magnetism with the V_{Si}-V_C divacancies. In a followup work by Wang *et al.* [52], a much broad range of neutron fluence was applied. It was found that the paramagnetic component dominates and the ferromagnetic component is relatively weak.

Almost at the same time, 6H-SiC single crystals have been shown to be ferromagnetic after bombardment using ions [53]. In this work, Ne^+ ions at an energy of 140 keV have been implanted at different fluence from 5×10^{13} to 1×10^{15} cm^{-2} denoted as 5E13...1E15, respectively. As shown in Fig. 11, the virgin SiC shows only diamagnetism. After Ne implantation (1E14), a ferromagnetic contribution appears. The as-measured magnetic moment is at the order of 10^{-4} emu for a sample of 5×5 mm^2. Note that the volume (sample thickness) affected by ion irradiation is much smaller compared with neutron irradiation. Figure 12 shows the ferromagnetic hysteresis loop after subtracting the diamagnetic background for samples with different fluences. An initial increase in structural disorder leads to pronounced ferromagnetic properties at room temperature. Further introduction of disorder reduces the saturation magnetization and at the same time the crystallinity of SiC is decreased. Close to the threshold of full amorphization [54], the saturation magnetization nearly drops to zero.

The picture from lattice damage to amorphization of SiC upon Ne ion implantation has been corroborated by Rutherford backscattering/channeling spectrometry (RBS/C). The ion-implantation-induced atomic disorder of the Si sublattice in 6H-SiC is quantitatively determined. Damage accumulation on the carbon sublattice is expected

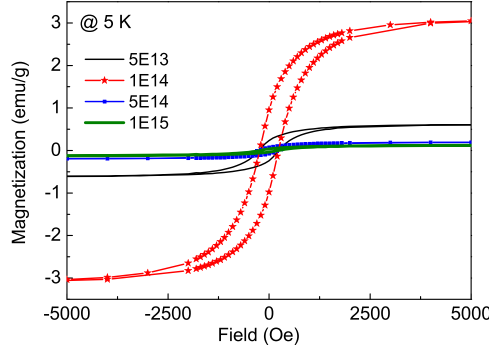

Figure 12. Magnetic properties measured at 5 K for 6H-SiC samples with different Ne ion fluences after subtracting the diamagnetic background. All samples were originally cut from the same wafer. The result has been published in Ref. [53].

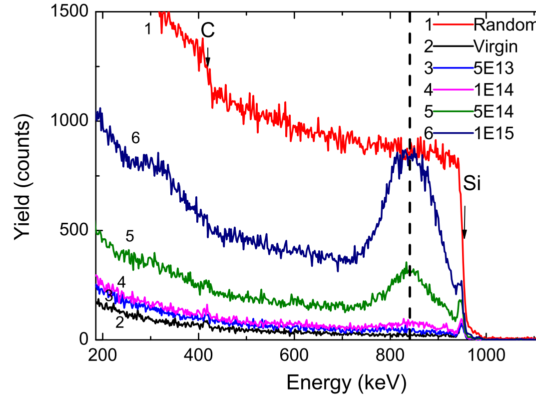

Figure 13. A sequence of 1.7 MeV He RBS/C spectra 6H-SiC single crystal implanted with 140 keV Ne ions at room temperature. A random spectrum and a channeling spectrum from a virgin sample are also included for comparison. The dashed line indicates the position of the Si damage peaks. Labels (5E13...1E15) mean the ion fluences, which are 5×10^{14}...1×10^{15} cm^{-2}. Results are partially published in Ref. [55].

to exhibit similar behavior according to SRIM full-damage cascade simulations. The RBS/C spectra along SiC[0001] are shown in Fig. 13 for the unirradiated (virgin) and for the same set of samples shown in Fig. 12. A random spectrum is also shown for comparison. The random spectrum is assumed equivalent to a completely amorphized SiC, while the virgin spectrum corresponds to an essentially damage-free crystal. The minimum yield χ_{min}, defined as the ratio of the virgin spectrum to the random spectrum, is 2.3% for the 6H-SiC crystals at the surface region. At the ion fluence of 5×10^{13} or 1×10^{14} cm^{-2}, the yield in the channeling spectrum is only slightly higher than the virgin sample, indicating the detection threshold of RBS/C. A peak in the channeling spectrum becomes visible for fluences of 5×10^{14} and 1×10^{15} cm^{-2}. The damage peak is estimated to occur at a depth of 150 nm, in agreement with SRIM simulations. At the damage

peak, χ_{min} is calculated to be 5.0%, 8.4%, 33% and 93% for different fluences (*dpa*). At the same depth, χ_{min} is 2.6% for the virgin crystal. Note that for the fluence of 1E15 (corresponding to the peak *dpa* of around 0.5), χ_{min} is 93%, indicating the almost full amorphization at the damage peak. Compared with the magnetization data in Fig. 12, there is a narrow fluence window, within which the sample is ferromagnetic. The initial introduction of structural disorder leads to pronounced magnetization. Further increasing disorder induces the amorphization of the host SiC crystal and therefore decreases the saturation magnetization. This is in agreement with the threshold dpa values for amorphization reported in literature [54].

In both papers [48, 53] about ferromagnetism in neutron and ion irradiated 6H-SiC, it is tentatively proposed that V_{Si}-V_C divacancies form local magnetic moments and those local moments ferromagnetically order due to the extended tails of the defect wave functions [48]. As an important technologic material, SiC is commercially available at large scale and with high quality. There are many groups utilizing ions to induce defects and to study magnetic properities in SiC with different polytypes [56, 57, 58, 59, 60, 61]. Different defects, such as V_{Si} [59], are also proposed to be responsible for the ferromagnetism.

3.2. Paramagnetism

As shown in Fig. 8, after neutron irradiation, the diamagnetic background becomes less pronounced. If one checks the field dependence of the magnetization (for the sample with the fluence of 2.29×10^{18} n/cm^2), it is like a Brillouin function. In Ref. [52], a detailed study over a larger range of neutron irradiation fluence and temperature dependent magnetization was presented. Samples were commercial semi-insulating 4H-SiC single crystal wafers from Cree. Particle induced X-ray emission (PIXE) was performed to check magnetic impurities in the pristine sample. The concentrations of magnetic impurities (Fe, Co and Ni) are below the detection limits of about 1 ppm. Neutron irradiation was performed at chambers DBVK and DBVR at the BER II reactor at Helmholtz-Zentrum Berlin. Since thermal neutrons only produce negligible displacement, only epithermal and fast neutrons are counted in the fluence calculation [30]. The neutron fluence spanned a large range from 3.28×10^{16} cm^{-2} to 3.50×10^{19} cm^{-2} covering all possibilities from light damage to near amorphization. It is worthy to note that the applied neutron fluence covers the range used in Ref. [48] and is extended to much higher fluence values by two orders of magnitude.

Figure 14 shows the magnetic properties measured at 5 K of the virgin 4H-SiC and a sample irradiated with neutrons with a fluence value of 4.68×10^{17} cm^{-2}. Here, the results are displayed without any background subtraction but only normalized by the mass of the samples. The difference between the virgin and irradiated SiC is clear to see: the virgin SiC shows purely diamagnetic behavior, while the irradiated one reveals a large deviation from the linear dependence on the magnetic field, which is the contribution from the paramagnetic component. The inset of Fig. 14 shows the zoom of

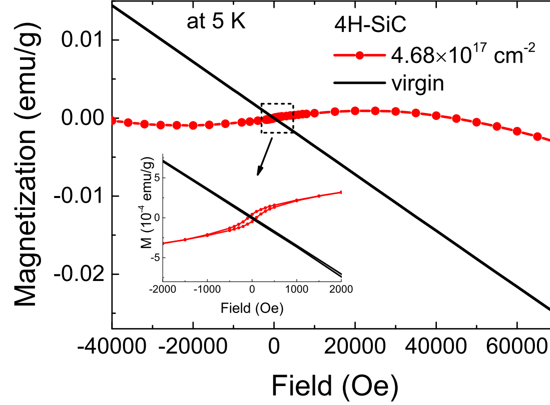

Figure 14. Magnetic properties: virgin vs. neutron irradiated 4H-SiC. Inset: the zoom of the low field range. Figure is from Ref. [52].

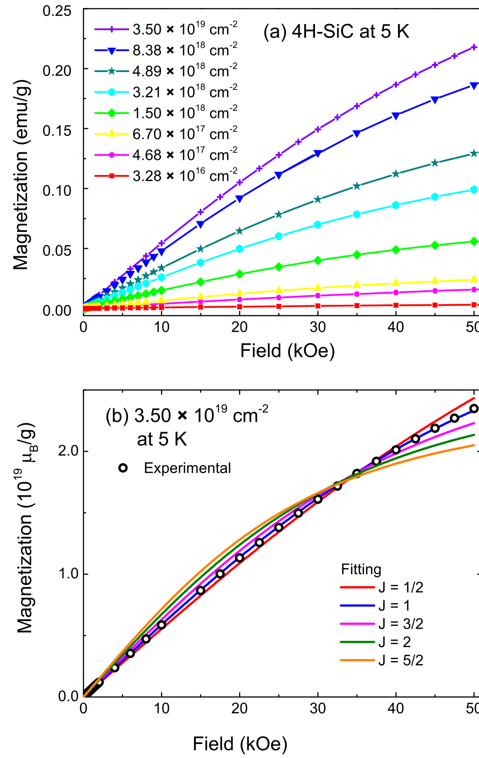

Figure 15. (a) Magnetization of neutron irradiated samples measured at 5 K as a function of field [$(M(H)$]. The numbers label the neutron fluences. The diamagnetic background has been subtracted. (b) Fits of the magnetization measured at 5 K for the sample with a fluence of 3.50×10^{19} cm^{-2} using the Brillouin function with different values of J. Figures are from Ref. [52].

the low field part. A ferromagnetic contribution is also induced by neutron irradiation with its saturation magnetization around 1% of the paramagnetic signal.

In order to quantify the paramagnetic centers induced by neutron irradiation, the

diamagnetic background has to be carefully subtracted. One can use the diamagnetism measured at higher temperature (here 300 K) for the virgin sample to approximate the diamagnetic background in all samples. Figure 15(a) shows the magnetization [*(M(H)*] of neutron irradiated SiC after subtracting the diamagnetic background. All samples exhibit a paramagnetic component and the magnetization increases with increasing neutron fluence. The paramagnetism can be described by Brillouin function:

$$M(\alpha) = NJ\mu_B g[\frac{2J+1}{2J}coth(\frac{2J+1}{2J}\alpha) - \frac{1}{2J}coth(\frac{\alpha}{2J})], \quad (1)$$

where the g factor is about 2 as obtained from electron spin resonance measurement [52], μ_B is the Bohr magneton, $\alpha = gJ\mu_B H/k_B T$, k_B is Boltzmann constant and N is the density of spins.

As exemplarily shown in Fig. 15(b), the data can be fitted nicely by $J = 1$. A larger or smaller J results in a pronounced deviation from the experimental data. This fitting hints that the measured paramagnetism is due to defects with moment $\mu = gJ\mu_B = 2\mu_B$. This conclusion is in excellent agreement with our first-principles calculation (shown in Section 3.4): the induced magnetism is due to V_{Si}-V_C divacancies which carry a magnetic moment of $2\,\mu_B$. As a comparison, the induced magnetism in graphite is generally attributed to single vacancy [62, 63, 64, 65].

Figure 16 presents the temperature dependent magnetization [*M(T)*] for samples with different neutron fluences under an applied field of 10000 Oe. The diamagnetic background is essentially temperature independent and therefore dominates at higher temperature. The Curie-like paramagnetic component shows a strong dependence on temperature and neutron fluence. Self-consistently, the *M(T)* curves can be well fitted according to the Curie law (Eq. 2) by using the same J and N obtained from the corresponding *M(H)* curve fitting: $J = 1$ and $N = 1.66\times10^{19}$/g for the sample shown in Fig. 15(b) and Fig. 16(b).

$$\chi = \frac{M}{H} = N\frac{J(J+1)(g\mu_B)^2}{3k_B T} \quad (2)$$

It has been shown that thermal annealing can heals partially the induced defects. The removal of defects is reflected by the magnetization measurements. As shown in Fig. 17, the magnetization of irradiated SiC is reduced gradually after thermal annealing at different temperature.

The paramagnetism in defective SiC was also revealed in nanocrystalline SiC [66]. The magnetization of the films is correlated with the deposition temperature. At higher deposition temperature, the magnetization becomes lower. The authors concluded that the magnetism in nanocrystalline SiC films is from neutral charged V_{Si}-V_C divacancies.

3.3. Magnetic phases in ion irradiated SiC

As shown in the preceding two sections, both paramagnetism and ferromagnetism can be detected in defective SiC. In principle, paramagnetism or the appearance of local

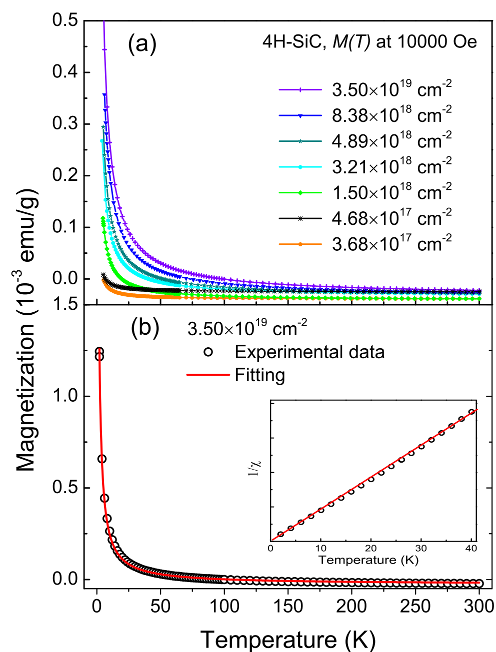

Figure 16. (a) The magnetic moment of neutron irradiated 4H-SiC samples measured under a magnetic field of 10000 Oe as a function of temperature [$M(T)$]. The numbers label the neutron fluences. (b) Fitting by equation 2 for the sample irradiated with the largest fluence: the black symbols are experimental data and the red solid curve is the fitting result. Figure is from Ref. [52].

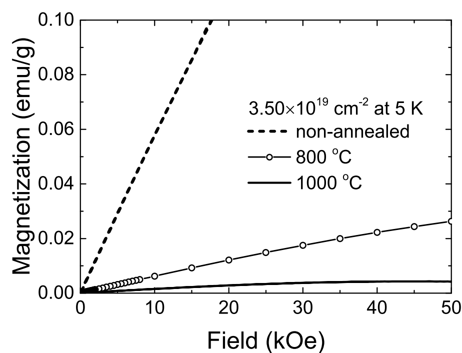

Figure 17. Magnetization of irradiated 4H-SiC after annealing at different temperatures: measurements at 5 K as a function of field [$(M(H)$]. Figure is adapted from Ref. [52].

moments is the prerequisite for ferromagnetism (the result of interaction between local moments). Therefore, in ion irradiated SiC, in which the defects are not uniformly distributed, there should be a mixed magnetic phases including paramagnetism and ferromagnetism. However, paramagnetism is weak and difficult to detect.

A careful analysis was done for Ne irradiated 6H-SiC [67]. Figure 18(a) shows the comparison of the hysteresis loops measured at 5 K for the virgin SiC and for sample 1E14. The implantation energy was 140 keV and the sample label 1E14 means the ion fluence of 1×10^{14} cm^{-2}. In Fig. 18(b), we display the magnetization of sample 1E14 after removing the diamagnetism and the paramagnetism from the substrate. After this treatment, the paramagnetic part can be mostly subtracted, but not completely. The slightly increased magnetization with field at the large-field part (shown in Fig. 18(b)) indicates a paramagnetic contribution in the irradiated sample.

Figure 19 shows the hysteresis loops of sample 1E14 measured at different temperatures. One can observe three features: (1) the hysteresis persists above room temperature, (2) there is only a slight decrease of the saturation magnetization, and (3) the coercivity changes at different temperature range. The coercivity drops from 260 Oe at 5 K to 130 Oe at 50 K, and then drops slowly with increasing temperatures. These features indicate the co-existence of ferromagnetism and superparamagnetism [68, 69, 70].

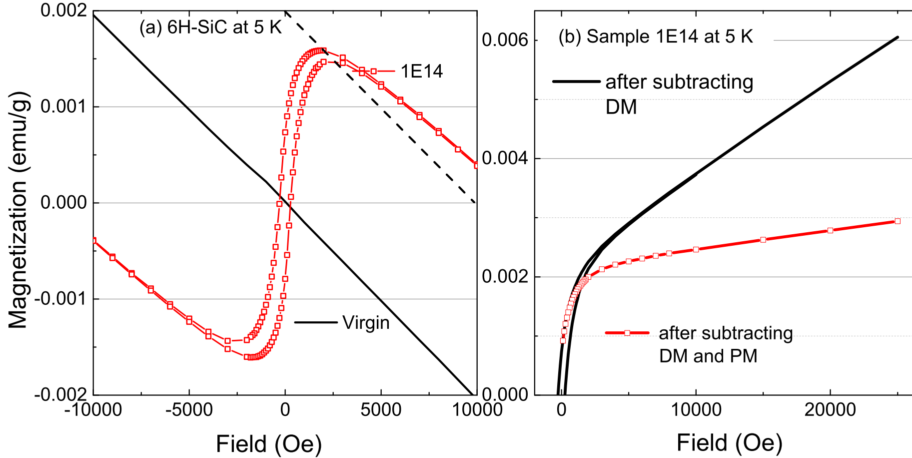

Figure 18. (a) The hysteresis loops measured at 5 K for the virgin 6H-SiC (single crystal) and sample 1E14. The dashed line is a guide for the eye to show the diamagnetic background from the substrate. (b) Magnetization at 5 K of sample 1E14 after subtracting different contributions from the substrate. DM: diamagnetism and PM: paramagnetism. The magnetization is normalized by the whole sample mass. To subtract the PM contribution, only 1/4 of the hysteresis data were numerically processed. Figures are adapted from Ref. [67].

It is unrealistic to calculate separate hysteresis loops for the ferromagnetic and superparamagnetic components. But the magnetic remanence and coercivity for the superparamagnetic component show different behavior compared with ferromagnetism

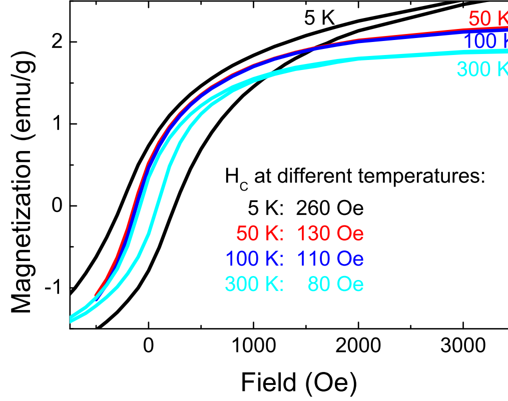

Figure 19. Hysteresis loops at different temperatures for sample 1E14 (single crystalline 6H-SiC). Note that only a half loop was measured at temperature 50 and 100 K. One can see a fast drop of the coercivity from 5 K to 50 K, but a slower decrease above 50 K. The magnetization is normalized by the mass of the implanted layer corresponding to around 0.1% of the sample. Figure is from Ref. [67].

upon increasing temperature. Therefore, one can analyze the temperature dependent magnetic remanence to decompose it into different components as shown in Fig. 20. For superparamagnetism, the remanence and coercivity are more sensitive to temperature [69]. As shown in Fig. 20, the magnetic remanence measured at 10 Oe (a small field to compensate the possible trapped field in the superconductor magnet of the measurement setup) shows two distinct regimes with increasing temperature: it decreases rapidly below 50 K and moderately above 50 K. This is consistent with the coercivity change with increasing temperature shown in Fig. 19. The temperature dependence of magnetization for superparamagnetism and single-phase ferromagnetism can be described by their sum [71]:

$$M = M_s(0)[1 - (T/T_c)^{3/2}] + n\mu[coth(\mu H/k_BT) - k_BT/\mu H], \tag{3}$$

The first term represents the spontaneous magnetization of the ferromagnetic component at temperatures below the Curie temperature and the second refers to the superparamagnetism. For the first term, T_C is the Curie temperature, $M_S(0)$ is the spontaneous magnetization at 0 K, and k_B is the Boltzmann constant. For the second term, n is the density of superparamagnetic clusters and μ is the average magnetic moment of one superparamagnetic cluster.

As shown in Fig. 20, the temperature-dependent magnetization can be well fitted by considering both superparamagnetism and ferromagnetism contributions. For superparamagnetism the spontaneous magnetization can only appear below the blocking temperature. For both samples, the contribution from the superparamagnetic component drops to zero at temperature slightly above 50 K. For sample 1E14, the fitting results show that one superparamagnetic cluster contains around 8.1×10^4 μ_B. According to the theoretical calculation [48], each divacancy generates $2\,\mu_B$. Assuming

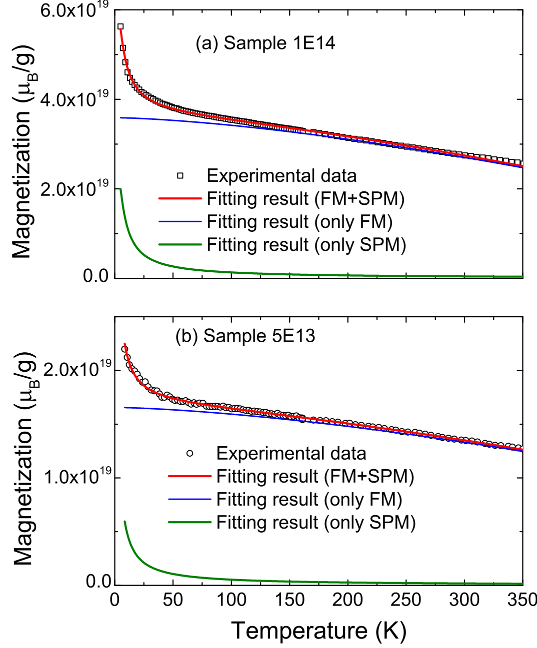

Figure 20. Magnetic remanence of Ne irradiated 6H-SiC samples: one can see the large difference of the magnetization vs. temperature at temperature below and above 50 K. The data are shown without considering the diamagnetic and paramagnetic background which is negligible due to the small field. The solid lines are fits according to Eq. 3. Figure is from Ref. [67].

the magnetic moments arising from $V_{Si}V_C$ divacancies, one magnetic cluster in sample 1E14 contains around 40000 $V_{Si}V_C$ divacancies, however, it is difficult to correlate it to a physical cluster size. For the ferromagnetic contribution, the best fitting gives T_C of around 760 K. Although the saturation magnetization is different for samples 5E13 and 1E14 (see Fig. 18), both samples show a similar behavior in the temperature-dependent magnetic remanence. The ferromagnetic component of sample 5E13 is deduced to also have a T_C around 750 K, implying that the magnetic properties in both ion irradiated SiC samples have the same origin.

The coexistence of different magnetic phases can also be concluded by the zero field cooled/field cooled (ZFC/FC) measurements as shown in Fig. 21. The ZFC magnetization was measured by cooling the sample from 300 K to 5 K under zero field, then a field of 100 Oe was applied and the magnetization was measured during warming up. The FC curves were measured by cooling the sample in a field of 10000 Oe, then at 5 K the field was decreased to 100 Oe and the magnetization was measured also during warming up. The ZFC/FC curves for both samples are different from those of samples with a single magnetic phase. For a superparamagnetic system (*e.g.* magnetic nanoparticles) the ZFC curve would increase with temperature, peak at a particular

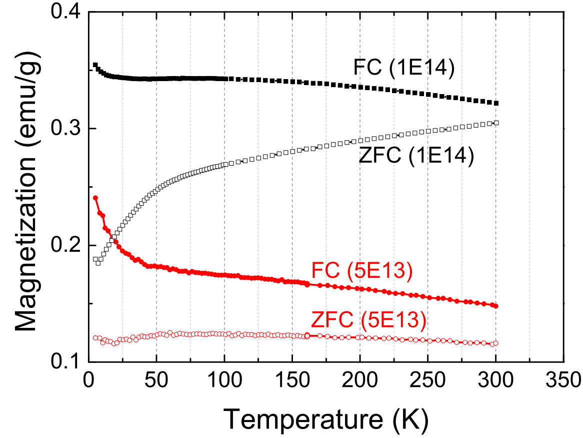

Figure 21. ZFC/FC magnetization for two irradiated 6H-SiC samples with Ne ion fluences of $5\times10^{13}/\text{cm}^2$ (5E13) and $1\times10^{14}/\text{cm}^2$ (1E14), respectively. The thermal irreversibility has been observed for both samples. The data are shown without subtracting the diamagnetic and paramagnetic background which is negligible at the applied small field. Figures are from Ref. [67].

temperature range and finally merge with the FC magnetization. For a ferromagnetic system, when the coercivity is larger than the applied field, the ZFC magnetization can be very small compared with the FC magnetization and temperature-independent below the Curie temperature. When the coercivity is small, the ZFC curves superimpose on the FC curves [72]. For both SiC samples shown in Fig. 21, the ZFC/FC curves cannot be explained by a single magnetic phase. They can only be understood, if assuming a superparamagnetic phase with blocking temperature around 50 K and a ferromagnetic phase with Curie temperature well above 300 K.

To understand the co-existence of paramagnetism, superparamagnetism and ferromagnetism in ion irradiated SiC, we can consider the following facts: (1) the defects in SiC are non-homogenously distributed, (2) the isolated, uncoupled defects contribute to the paramagnetism and (3) the coupled defects result in the superparamagnetic and ferromagnetic components. The ferromagnetic coupling is expected to first appear within regions with proper defect concentrations. Some regions are connected to be big enough and behave as a ferromagnet. Some regions with ferromagnetically coupled defects are small and behave as superparamagnets. In a recent work about Gd-doped GaN [73], Thiess *et al.* found that intrinsically the Ga vacancies tend to cluster, leading to the co-existence of ferromagnetism and superparamagnetism. This scenario could also explain the experimental results in ion irradiated SiC.

Such a co-existence of different magnetic phases including paramagnetic, superparamagnetic and ferromagnetic components has been also identified in nano-crystalline SiC with defects [66], in reduced graphene oxide [74] and in irradiated graphite [75, 76].

3.4. Coupling mechanism (First principles calculations)

To understand the formation of local moments and the magnetic coupling between them, first-principles calculations are indispensable. One early attempt has been done for 3C-SiC. In Ref. [77], the author addressed the interactions between Si vacancies V_{Si} in 3C-SiC. High-spin configurations are predicted for the negatively-charged V_{Si} defects. Ferromagnetic coupling is possible when V_{Si} defects are at -2e charge state, while V_{Si} defects at -e charge state tend to order antiferromagnetically. The authors proposed to use nitrogen doping to manipulate the charge states of V_{Si} and thereby the magnetic interactions between them. When the N:V_{Si} ratio is near 1:1, V_{Si} is at the high spin ground state with a local magnetic moment of $3\,\mu_B$ and interacts with each other antiferromagnetically. When the N:V_{Si} ratio is around 2:1, V_{Si}-induced local magnetic moments are $2\,\mu_B$ per vacancy and they couple ferromagnetically. N-ion implantation was done experimentally for 6H-SiC [59]. Both ferromagnetism and V_{Si} were detected in the sample, supporting the first-principles calculations. However, in another work N-implantation induced much weaker magnetism than Al-implantation in 4H-SiC [78].

For neutron irradiated 6H-SiC [48], V_{Si}-V_C divacancies were identified. First-principles calculations revealed that V_{Si}-V_C divacancies can lead the formation of local moments and the extended tails of defect wave functions make long-range ferromagnetic coupling possible. The calculated spin-resolved density of states (DOS) of the 192-atom supercell [see Fig. 22(a)] shows that each neutral axial (*hh*) V_{Si}-V_C yields a magnetic moment of $2.0\,\mu_B$. The spin-polarization energy, the energy difference between the spin-polarized and spin-unpolarized states, was calculated to be 1.90 eV, meaning that the spin-polarized state is stable well above room temperature. The spin polarization induced by the neutral V_{Si}-V_C leads to a 0.50 eV splitting between the majority- and minority-spin states. Figure 22(b) shows the charge density isosurface of defect states associated with a neutral V_{Si}-V_C in the 192-atom supercell. It demonstrates both the localized nature and the extended tails of the defect wave functions beyond the supercell.

If doubling the size of the supercell by putting two 192-atom cells side by side, one can estimate the magnetic coupling (ferromagnetic or anti-ferromagnetic) between the V_{Si}-V_C-induced local moments. The energy difference between the antiferromagnetic and ferromagnetic phases is E_{AFM}-E_{FM}=$8J_0S^2$ according to the nearest-neighbor Heisenberg model, where J_0 is the nearest-neighbor magnetic coupling and S is the net spin of the defect states. A negative J_0 means that AFM is energetically favored and otherwise FM favored. The calculation results show that when the divacancies V_{Si}-V_C in 6H-SiC is separated by 12.3 Å, J_0 is -9.8 meV for neutral charge (0, 0) state, 8.4 meV for (+1, +1) and 34.1 meV for (-1, -1) charge states.

To investigate how the spin-polarization energy and the J_0 depend on the defect concentration, more detailed calculations have been done for 4H-SiC [52]. The spin-polarizing energies ΔE_{sp} of supercells as a function of d_V are shown in Fig. 23. d_V is defined as the distance between adjacent axial (*hh*) V_{Si}-V_C in the *a*-*b* plane. It is found that ΔE_{sp} increases when d_V increases, indicating that the spin polarization is more

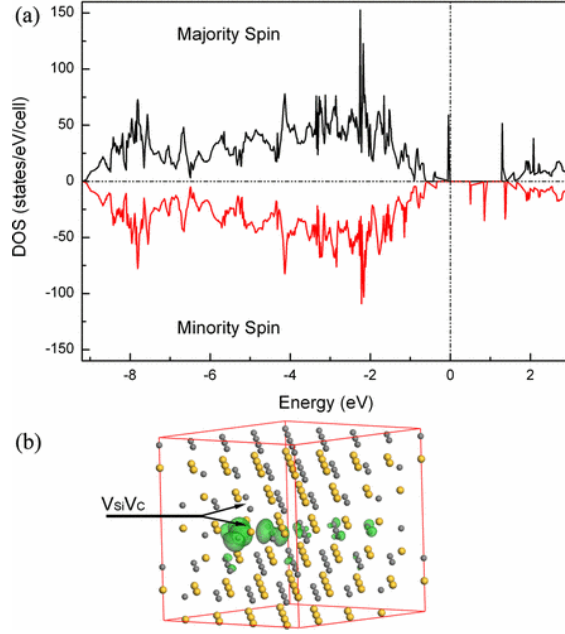

Figure 22. (a) Spin-resolved DOS of a neutral axial (*hh*) V_{Si}-V_C in a 192-atom 6H-SiC supercell. The spin polarization leads to a splitting between two kinds of spin states. (b) Isosurface charge density plot (the isovalue is $0.02\, e/\AA^3$) of the total spin states about a neutral V_{Si}-V_C in a 192-atom SiC supercell, showing both the localized nature and the extended tails of the defect wave functions. Si atoms are shown in yellow and C atoms in gray. Arrows indicate the location of V_{Si}-V_C. Figures are from Ref. [48].

stable under low V_{Si}-V_C concentrations. When d_V is larger than 9.7 Å, ΔE_{sp} changes from negative to positive and the spin polarization becomes energetically favored. Here, the supercells with d_V less than 9.7 Å are designed to obtain the critical value of d_V switching the sign of ΔE_{sp}. Besides, each V_{Si}-V_C yields a local moment of $2.0\,\mu_B$ when d_V is more than 12.34 Å. This result is in well agreement with the experimental data shown in Figs. 15 and 16. The experimental results show that the induced paramagnetism is due to a single species with moment of $2\,\mu_B$.

Table 2 displays the calculated J_0 for different d_V and charge state. V_{Si}-V_C does not couple with each other along the *c* axis, even when d_V is as small as 10.11 Å. The exchange interaction is much stronger along the *a* axis and strongly depends on the charge state. Neutron or positively charged V_{Si}-V_C antiferromagnetically couples with a maximal exchange interaction of 125.68 meV when d_V is 12.33 Å. Negatively charged V_{Si}-V_C divacancies favor a ferromagnetic coupling. However, the exchange interaction dramatically decreases from 49.36 meV to 3.71 meV when d_V is increased from 12.33 to 18.50 Å.

In Figure 23(b), we plot the ferromagnetic exchange interaction energy as a function of d_V. As shown in Fig. 23(a) and (b), the ferromagnetism induced by divacancies requires that divacancies are negatively charged with d_V in the range from 12.33 Å to 15.42 Å. The required d_V would correspond to a concentration of divacancies in the order

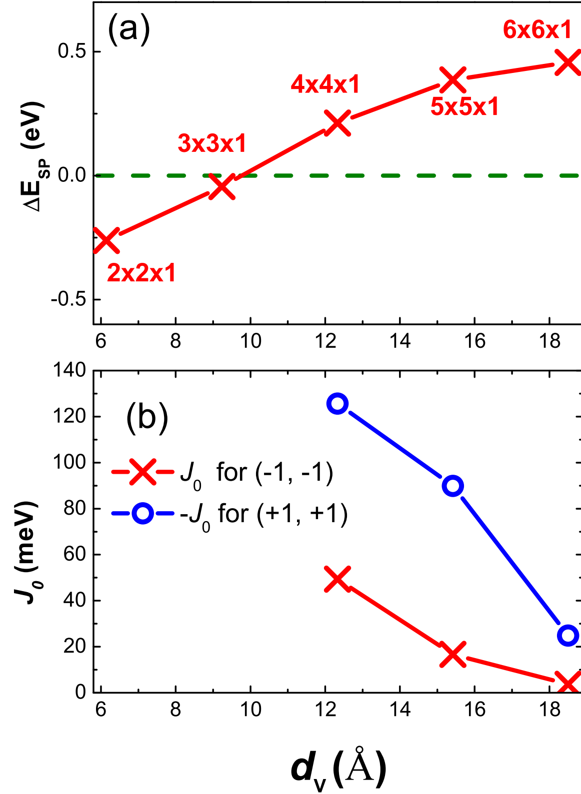

Figure 23. (a) Spin-polarization energy ΔE_{sp} as a function of the distance d_V between the adjacent axial (hh) divacancies in 4H-SiC. ΔE_{sp} increases with increasing d_V and the critical value is 9.7 Å. The corresponding supercell structures with one V_{Si}-V_C are marked with the numbers and multiplication signs. (b) The ferromagnetic (or antiferromagnetic) exchange coupling energy between charged (-1, -1) or (+1, +1) divacancies as a function of d_V. Figures are from Ref. [52].

of 3–6$\times10^{20}$ cm^{-3} ($1/d_V^3$). This concentration is well above the maximum concentration for the local moments obtained by neutron irradiation [52]. However, after irradiation with the largest neutron fluence the sample is approaching amorphous and the density of paramagnetic centers (N) starts to saturate. In this sense, it is unrealistic to expect the ferromagnetic coupling throughout the whole bulk sample. The experimentally observed weak ferromagnetism can be understood as a local effect: only some regions with nm or μm dimension can accommodate a high concentration of divacancies. These regions form ferromagnetic bubbles with very strong interaction (see Table 2), leading to the high Curie temperature. Presumably, these regions could be surface, interface or grain boundary. However, according to our calculation the spin-polarization will be unfavorable if d_V is too small. Therefore, the narrow fluence window of ferromagnetism shown in neutron irradiated SiC [52] as well as in neon implanted SiC [53] can be understood: For samples irradiated with low fluences, some local regions accommodating

Table 2. Magnetic coupling between axial (*hh*) V_{Si}-V_C-induced local moments in 4H-SiC. The coupling is antiferromagnetic between neutral or positively charged V_{Si}-V_C while ferromagnetic between negatively charged ones. When the alignment direction of V_{Si}-V_C is along *c* axis, the coupling almost does not exist. Results are from Ref. [52].

d_V (Å)	*c*- or *a*-axis	charge state	E_{AFM}-E_{FM} (meV)	J_0 (meV)
10.11	*c* axis	(0, 0)	-0.55	-0.14
12.33	*a* axis	(0, 0)	-39.45	-4.93
12.33	*a* axis	(+1 +1)	-251.35	-125.68
12.33	*a* axis	(-1, -1)	98.73	49.36
15.42	*a* axis	(0, 0)	-5.77	-0.72
15.42	*a* axis	(+1, +1)	-179.81	-89.90
15.42	*a* axis	(-1, -1)	33.31	16.66
18.50	*a* axis	(0, 0)	-0.93	-0.12
18.50	*a* axis	(+1, +1)	-49.75	-24.88
18.50	*a* axis	(-1, -1)	7.43	3.71

a larger concentration of divacancies appear to be ferromagnetic. When d_V in the local regions reaches the critical value of 9.7 Å, the increase of irradiation fluence (defect concentration) will suppress the spin polarization. There may appear some new local regions with the concentration of divacancies reaching to the level to induce ferromagnetism, but the damage to the crystalline structure by irradiation will weaken the coupling. Therefore, the amount of paramagnetic centers can be scaled up with neutron fluence and shows saturation at very large fluences.

For SiC nano-structures, the situation can be different. Morbec *et al.* investigated the effects of vacancies on the magnetic properties of zigzag SiC nanoribbons (Z-SiCNR) by using *ab initio* calculations based on density functional theory [79]. Single (V_C and V_{Si}) and double ($V_{Si}V_{Si}$ and V_{Si}-V_C) vacancies are found to induce magnetism in Z-SiCNRs. A single V_C can lead to a transition from half-metallic to metallic behavior in Z-SiCNRs due to the edge Si *p*-orbitals and the atoms surrounding the vacancy. Foreign impurity atoms (B and N) can interact with vacancies. The formation energies of vacancies can be reduced by substitutional B and N atoms. Ferromagnetism can be expected if Z-SiCNRs are grown under proper conditions.

3.5. Microscopic origin

In the previous sections, we have shown that divacancies V_{Si}-V_C are the dominating defect type in neutron and ion irradiated SiC. Note that the nearest-neighbor atoms of V_{Si}-V_C include three carbon atoms as well as three silicon atoms. It is therefore interesting to clarify where the local moments reside on. X-ray absorption near-edge structure (XANES) and X-ray magnetic circular dichroism (XMCD) are element-specific techniques and have been used to measure the magnetic contribution from different elements with partially occupied $3d$ or $4f$ subshells [80, 81]. Ohldag et al. [82] applied

XMCD to investigate the magnetism at the carbon K-edge in proton irradiated highly oriented pyrolytic graphite (HOPG). XANES was used to investigate the bonding state in SiC single crystals [83]. Therefore, it is possible to understand the microscopic picture about the defect-induced ferromagnetism in SiC by using soft X-ray spectroscopy.

Figure 24(a) shows the XANES spectra of the silicon K-edge for 6H-SiC. Comparing with the pristine sample, the peak positions of irradiated samples are not changed, but the relative strength of the peak at 1848 eV decreases, which suggests an increase of defect density [83]. As shown in Fig. 24(b), the XMCD signal is within the detection noise level in both the pristine sample and the sample 5E12 (The sample was implanted with Xe ions at 500 keV to a fluence 5×10^{12} cm^{-2}) at the silicon K-edge. No spin-polarized states close to the Fermi level occur at silicon atoms, and thus silicon centers do not contribute to the ferromagnetism observed in sample 5E12. Figure 24(c) shows the XANES spectra at the carbon K-edge of sample 5E12 and the pristine sample measured at 300 K. Resonances around 285 eV and 290 eV are attributed to the transition of carbon $1s$ core-level electrons to π^* and σ^* bands, respectively [82]. The resonance at 285 eV of the sample 5E12 is sharper than that of the pristine sample. The orbital hybridization at carbon is modified from the diamond-like sp^3-type carbon in pure 6H-SiC towards a more planar, graphitic sp^2-type carbon center, which leaves the orthogonal p_z orbital unchanged and gives rise to the peak of π^* bands [84]. This feature indicates a change of the local coordination from the tetrahedrally coordinated carbon atom in pristine SiC to the three-fold bound carbon site. In sharp contrast to the silicon K-edge, a sizeable XMCD signal appears at the carbon K-edge as shown in Fig. 24(d). Therefore, we can conclude that the defect-induced ferromagnetism originates from a spin-polarized partial occupancy of the p_z orbitals at carbon atoms close to defect sites in SiC.

In Ref. [50], first-principles calculations were employed to understand why the magnetic signal observed only from carbon atoms. As shown in Figure 25(a), 90% of the spin polarization is contributed by the valence states of the carbon atoms. This explains why XMCD is only observed at the carbon K-edge. Further, by comparing the partial spin-resolved DOS of nearest-neighbor carbon atoms with that of other carbon atoms, it is visible that 85% magnetic moments are from the three nearest-neighbor carbon atoms [see Figure 25(b)]. Therefore the magnetic moments of the nearest-neighbor carbon atoms of V_{Si}-V_C are mainly responsible for the ferromagnetism. In SiC, carbon has higher electronegativity than silicon and unpaired electrons will thus have a tendency to be attracted by carbon atoms. Spin polarization thus mainly appears at those carbon atoms around the vacancies. As shown in Fig. 25(c), our calculation indicates that most of the magnetic moments (90%) originate from the p states of nearest-neighbor carbon atoms of V_{Si}-V_C. Due to the attraction of the remaining adjacent silicon atoms, the nearest-neighbor carbon atoms will move away slightly from the V_{Si}-V_C divacancies. This structure change from the unperturbed four-fold bulk coordination to a more planar three-fold bound state is connected with rehybridizations at those C atoms in the close vicinity of V_{Si}-V_C. The distortion will modify the electronic structure locally towards a higher degree of sp^2 bonding orbitals and a singly occupied p-type lone pair at the

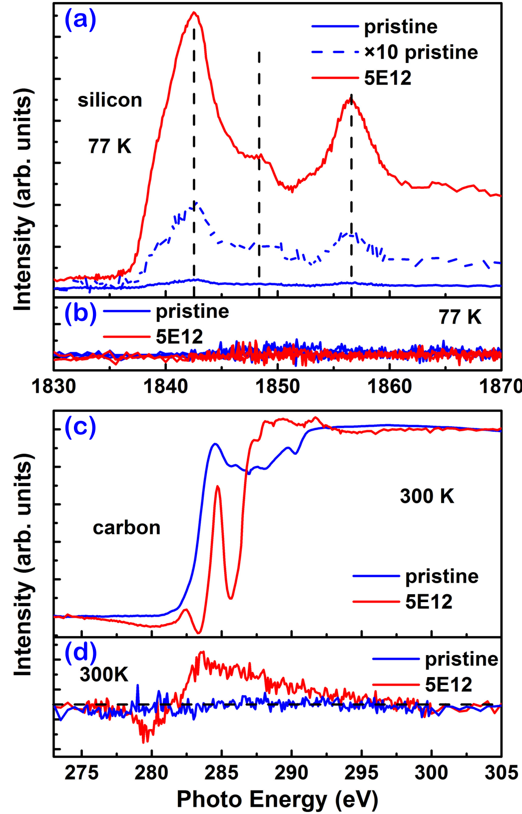

Figure 24. X-ray absorption spectra measured in EY (electron yield) mode for the sample 5E12 (the Xe irradiation fluence 5×10^{12} cm^{-2}) and the pristine 6H-SiC sample: (a) XANES of the silicon K-edge at 77 K, (b) XMCD at the silicon K-edge at 77 K, (c) XANES of the carbon K-edge at 300 K. (d) XMCD at the carbon K-edge at 300 K. Figures are from Ref. [50].

C atoms. Thus their outermost orbitals will acquire a significant π character and the magnetic moments are mainly contributed by p electrons, as shown in Fig. 25(d). The first-principles calculations corroborate well the interpretation of the XMCD experiment: the XMCD signal of SiC after irradiation is thus assigned to p electrons.

In another work, electron magnetic circular dichroism (EMCD) was used to measure the atomic origin of ferromagnetism in Al doped 4H-SiC [85]. EMCD was performed in transmission electron microscopy, measuring the difference in core-level electron energy loss spectra collected at two opposite chirality conditions. The same as XMCD, EMCD can detect the magnetic moments of a particular element. In the work by He et al. [85], EMCD signals were observed in C atoms in Al doped SiC, indicating that the spin polarization of C atoms contributes to the magnetic moments. It is in agreement with the XMCD study for ion irradiated 6H-SiC [50].

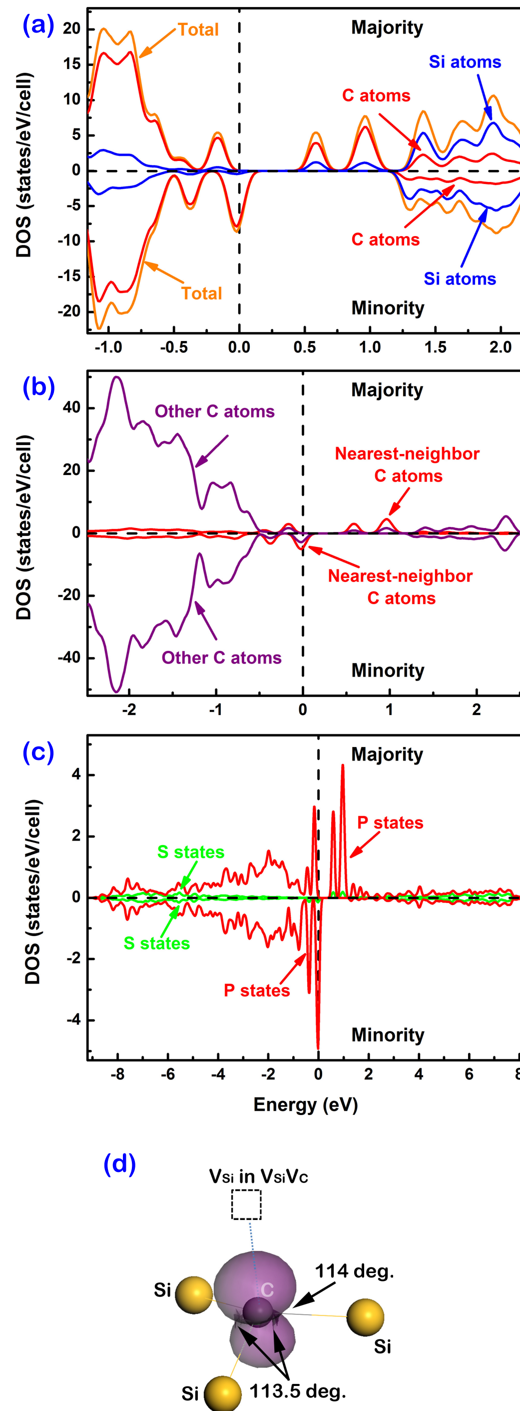

Figure 25. The electronic structure of $Si_{95}(V_{Si})C_{95}(V_C)$ (6H-SiC): (a) The total spin-resolved density of state (DOS) and the partial spin-resolved DOS of silicon atoms and carbon atoms, respectively. (b) Comparison of partial spin-resolved DOS of nearest-neighbor carbon atoms and others. (c) Comparison of the partial spin-resolved DOS of s and p electrons of nearest-neighbor carbon atoms of V_{Si}-V_C. (d) The structure and spin density isosurface ($0.08\,e/\AA^3$, in purple) around one of the nearest-neighbor carbon atoms. The carbon atom is in dark purple in the middle and silicon atoms are in yellow. The arrows indicate the bond angles of Si-C-Si. The dashed line and square symbol indicate the direction and the location of the adjacent silicon vacancy part (V_{Si}) within axial (hh) V_{Si}-V_C, respectively. The vertical dashed lines at zero indicate the Fermi energy. Figures are from Ref. [50].

3.6. Influence on nuclear spins

As a local probe technique, nuclear magnetic resonance (NMR) provides an impurity-insensitive way to get more insights into the magnetic properties of a material. In fact, NMR spectrum measures the on-site internal hyperfine fields in a sample. For SiC, one can use ^{13}C and ^{29}Si NMR spectroscopy to study the defect-induced paramagnetism in neutron irradiated 6H-SiC. The ^{29}Si and ^{13}C NMR spectra were acquired with a Hahn spin echo pulse sequence for temperatures 2–100 K at a magnetic field of $\mu_0 H = 7.100$ T. For the temperature dependent measurements, the magnetic field was applied in the wafer plane.

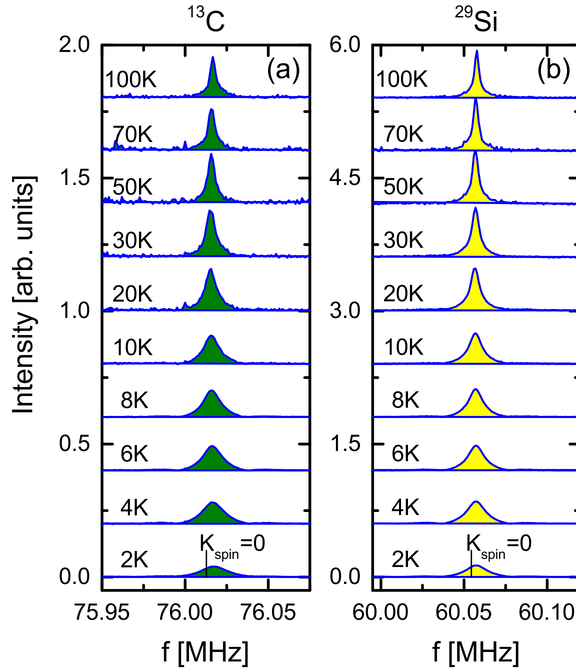

Figure 26. Experimental (a) ^{13}C and (b) ^{29}Si NMR spectra for the neutron irradiated 6H-SiC sample at different temperatures at a magnetic field of $\mu_0 H = 7.100$ T. The vertical markers over the spectra at 2 K label the frequency where $K_{spin} = 0$. Figures are from Ref. [86].

Figure 26 shows the experimental ^{13}C and ^{29}Si NMR spectra for the neutron irradiated 6H-SiC sample at temperature between 2 and 100 K. As expected, only one spectral line of the transition $I_z = -1/2 \rightarrow +1/2$ is observed for both isotopes due to their $I = 1/2$ nuclear spin state. The full width at half maximum (FWHM) of the spectra at 100 K is below 5 kHz, which is very small for a solid sample, indicating still high quality of the single crystal even after irradiation [52]. As the sample is cooled down, the FWHM becomes larger and is qualitatively attributed to the growing amplitude of the dipole magnetic field from the local moments of defects.

The NMR shift K is defined as $K = (f_{res} - f_0)/f_0$, where $f_0 = \gamma_n \mu_0 H/2\pi$ is the Larmor frequency of a bare nucleus with a gyromagnetic ratio γ_n in a magnetic

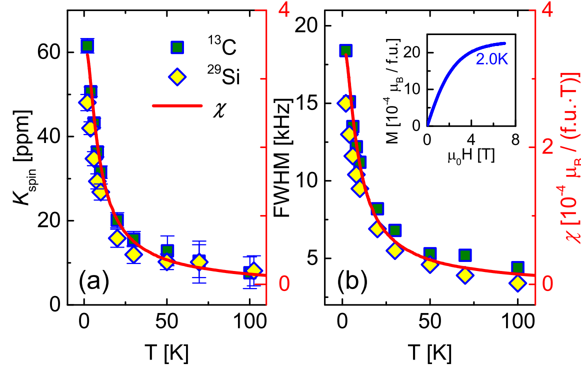

Figure 27. (a) Temperature dependence of spin part NMR shift K_{spin} for ^{13}C and ^{29}Si isotopes. (b) Temperature dependence of FWHM of ^{13}C and ^{29}Si NMR spectra. The identical red curves in (a) and (b) present the macroscopic susceptibility $\chi(T)$ ($\mu_0 H = 7$T), and the inset of (b) shows the magnetization as a function of applied field at 2 K. Figures are from Ref. [86].

field $\mu_0 H$, and f_{res} is the NMR frequency. K is a combination of a spin part and an orbital part originating from the orbital moment: $K = K_{spin} + K_{orb}$. K_{orb} is generally temperature-independent. The spin part $K_{spin} = A_{hf}\chi_{spin}$ is proportional to the static local susceptibility of the electronic spins at the nuclear site and to the hyperfine coupling A_{hf} between the nuclear spins and the electronic spins. The K_{orb} (or the $K_{spin} = 0$ reference frequency) can be obtained from very sharp ^{13}C and ^{29}Si NMR spectra at 100 K of an unirradiated 6H-SiC sample. K_{spin} carries the information of defect induced local moments.

The temperature dependence of the extracted K_{spin} and FWHM for both isotopes are shown in Fig. 27(a) and (b). The K_{spin} for both isotopes follows the Curie law, in agreement with the macroscopic magnetic susceptibility $\chi(T)$ of the electron spins. The paramagnetism is also characterized by the Curie law behavior of the FWHM for both ^{13}C and ^{29}Si isotopes, which gives a quantitative description of the growing amplitude of the dipole field of local moments with decreasing temperature. These results are clear evidence for the intrinsic paramagnetism in the neutron irradiated 6H-SiC.

In Fig. 28, we show the contour plot of the calculated K_{spin} in real space and the amplitude of K_{spin} is presented by colors. The local moments are indicated by the red-white-black singular points, where K_{spin} is divergently large but contributes little to the spectral weight due to their low volume fraction. The whole volume is split into positive and negative regions by the $K_{spin} = 0$ black contour lines. A larger positive K_{spin} volume is shown and results in a positive peak position in the spectrum. Moreover, a majority of the nuclear sites have an average distance of a few nanometers from a nearby local moment. All NMR measurements and simulations provide a clear picture of the microscopic magnetic properties of the SiC sample at atomic scale.

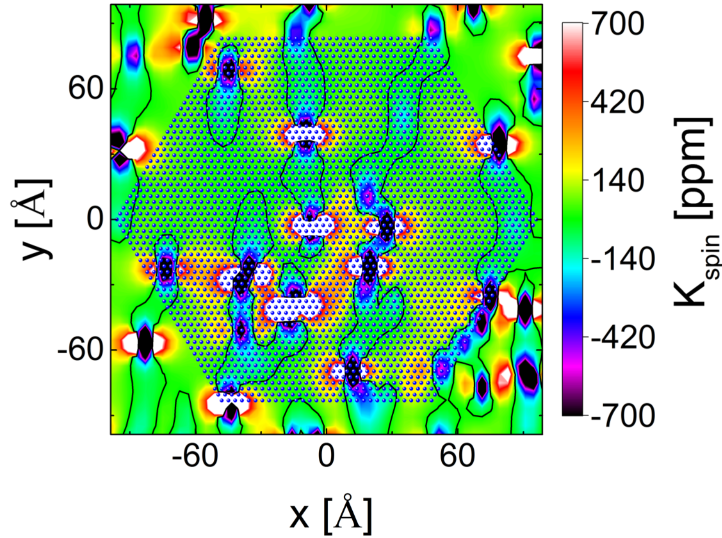

Figure 28. Simulation: contour plot of K_{spin} as a function of real space coordinates $(x, y, z = 0)$. Magnetic field is applied in plane, e.g. in x (or a) direction. The blue dots label the position of the nuclear sites, e.g. C atoms. The black solid lines label the positions where $K_{spin} = 0$. Figures are from Ref. [86].

4. Applications

4.1. Spintronics

The word "spintronics" (short for "spin electronics") refers to devices in which we can manipulate the spin degree of freedom in a similar manner as manipulating charge. Spintronic devices can drastically improve computation speed and reduce power consumption. Defect induced magnetism in semiconductors reveals high Curie temperature and in principle provides an alternative for dilute ferromagnetic semiconductors in spintronic applications. The prerequisite is the interaction between the magnetism and free carriers in semiconductors.

For SiC, one can implant Al or N dopants to create carriers and defects simultaneously. In Ref. [78], the authors investigated magnetic and transport properties in ferromagnetic 4H-SiC single crystals prepared by post-implantation pulsed laser annealing. The implantation energies for Al and N were 180 keV and 110 keV, respectively. Samples were implanted with fluences from 5×10^{13} to 5×10^{16} cm^{-2} for Al and from 1×10^{14} to 1×10^{17} cm^{-2} for N, respectively. Pulsed laser annealing was performed in ambient air with a 308 nm excimer laser with pulse duration of about 30 nanoseconds. The energy density was 0.2, 0.4, 0.6, 0.8 J/cm^2.

Figure 29(a) shows the magnetization vs. magnetic field in the range of 5 kOe at 5 K. Before annealing, only diamagnetic features can be observed in the as-implanted samples due to the heavy lattice damage [53]. After annealing with a low energy 0.2 J/cm^2, a weak hysteresis loop can be observed in a small field range. With increasing pulsed laser energies, the magnetic order gradually enhances. A distinct hysteresis

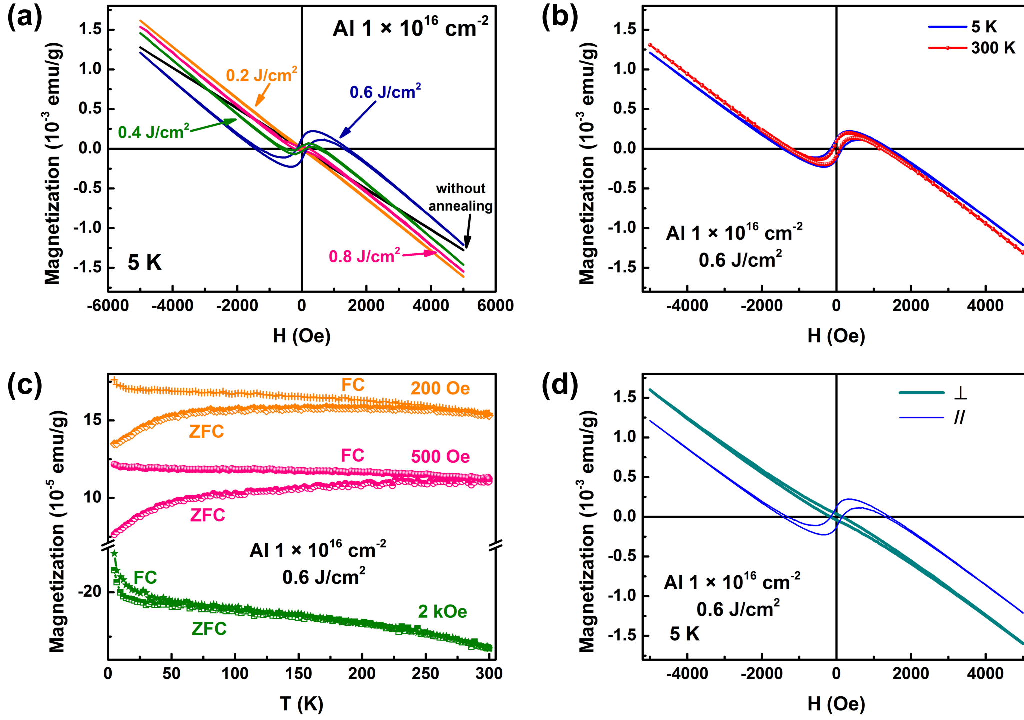

Figure 29. The magnetic properties of Al implanted 4H-SiC after pulsed laser annealing. (a) The magnetization as a function of magnetic field within 5 kOe at 5 K. (b) The magnetization vs. field for the sample annealed with the energy density of 0.6 J/cm^2 at 5 K and 300 K. (c) The zero field cooling (ZFC) / field cooling (FC) magnetization as a function of temperature from 5 K to 300 K under magnetic fields of 200, 500 and 2000 Oe. In (a-c) the magnetic field was applied parallel to the sample surface. (d) The magnetization as a function of magnetic field measured with the field both perpendicular and parallel to the sample surface (000-1) within 5 kOe. Clear magnetic anisotropy is observed. Figures are from Ref. [78].

loop with ferromagnetic features can be clearly seen and the saturation magnetization reaches 5×10^{-4} emu/g in the sample annealed using 0.6 J/cm^2. Then, the saturation in the 0.8 J/cm^2 decreases compared with that in 0.6 J/cm^2. At 300 K, the diamagnetism increases slightly while the hysteresis loop is similar as shown in Fig. 29(b). So the room-temperature ferromagnetism is induced by post-implantation annealing. The absence of tiny parasitic or any secondary magnetic phase is confirmed by the smooth and featureless magnetization vs. temperature curve [Fig. 29(c)]. Weak paramagnetism due to irradiation damage is also observed when the field of 2 kOe is applied. Figure 29(d) shows the magnetization measured with fields perpendicular and parallel to the sample surface (000-1), *i.e.* C face, at 5 K. The in-plane direction is found to be the easy axis. The *ab*-plane spin coupling is stronger than along the *c* axis, which could be the reason of this magnetic anisotropy [52]. Shape anisotropy is another contribution since the implanted layers are very thin. Nevertheless, the anisotropy corroborates that the magnetism is intrinsic, as foreign contamination or clusters unlikely bring either crystalline or shape anisotropy.

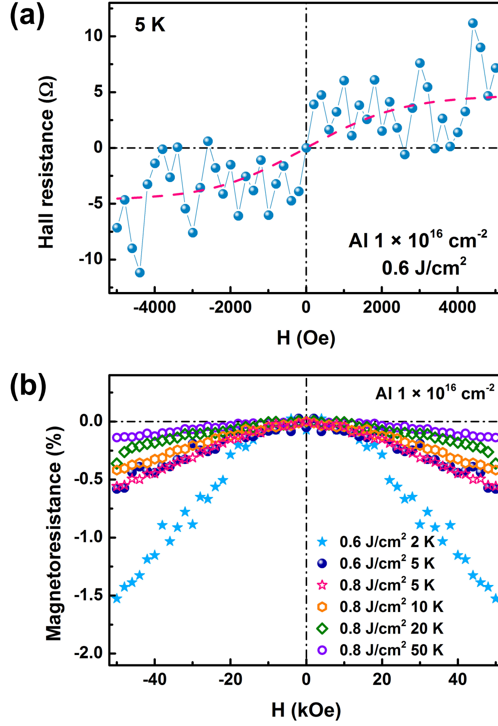

Figure 30. The magneto-transport properties of Al implanted 4H-SiC after pulsed laser annealing. (a) The Hall resistance of the 0.6 J/cm^2 sample with the field between $\pm$5 kOe at 5 K. The pink dashed line is a guide to the eye. (b) The magnetoresistance of the 0.6 J/cm^2 and 0.8 J/cm^2 samples in the field range of $\pm$50 kOe. Figures are from Ref. [78].

In the Hall effect measurement, the hole concentration and the mobility in SiC implanted with the Al fluence of 1×10^{16} cm^{-2} after 0.6 J/cm^2 pulsed laser annealing are estimated to be 3.4×10^{20} cm^{-3} and 0.40 cm^2/(Vs), respectively, while they are 2.3×10^{20} cm^{-3} and 0.02 cm^2/(Vs) for the 0.8 J/cm^2 sample. In the low field range, the trace of anomalous Hall effect is observed in Fig. 30(a). The weak and noisy signal is probably due to the low carrier mobility. Weak negative magnetoresistance is observed in the samples annealed with 0.6 J/cm^2 and 0.8 J/cm^2 shown in Fig. 30(b). Negative magnetoresistance of the 0.6 J/cm^2 sample can reach -1.5% under 50 kOe at 2 K, while at 5 K it is almost the same as that of the 0.8 J/cm^2 sample. The negative magnetoresistance decreases as the temperature increases and vanishes above 50 K. In contrast to Al implanted SiC, ferromagnetism is much weak in N implanted SiC.

The anomalous Hall effect and negative magnetoresistance show that the internal magnetic field from spin ordering can influence the behavior of carriers. So the interaction exists between moments induced by divacancies and carriers due to doping. However, the anomalous Hall effect is very weak. It is probably due to the fact that the defect-induced magnetism is weak and the carrier mobility is low.

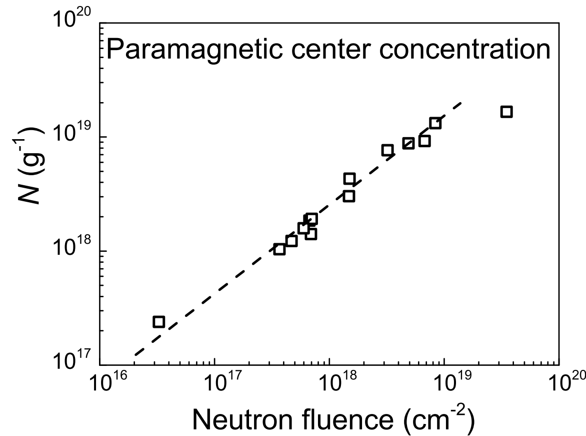

Figure 31. The fitted N (the density of paramagnetic centers) for 4H-SiC samples with different neutron fluence. The dashed line is only for guiding eyes to indicate the trend. The figure is adapted from Ref. [52].

4.2. Magnetometry as a measure of defects

As we shown in previous sections, the amount of paramagnetic centers is proportional to the concentration of defects. Therefore, paramagnetism in ion or neutron irradiated SiC can be taken as a quantitative measurement for defects. It is particularly useful when the amount of defects is rather low or not enough for some techniques, such as Rutherford backscattering spectrometry/channelling [87, 88, 89] and transmission electron microscopy [90, 1, 89, 52], due to their detection limits.

As an example, Figure 31 shows the concentration of paramagnetic centers (divacancies) depending on neutron fluence. The scaling between the concentration of paramagnetic centers and the neutron fluence provides a qualitative approach to measure irradiation induced defects by a magnetometry method. The concentration of defects increases with irradiation fluence, in agreement with the characterization by Raman. It is beyond the sensitivity of transmission electron microscopy to measure those point defects [52].

Figure 32 shows the paramagnetic component for Al implanted 4H-SiC. The paramagnetism also scales up with the Al fluence. The concentration of point defects, which is related to the density of paramagnetic centers, is determined by fitting the paramagnetic component of the specimen to the Brillouin function [91].

4.3. Magnetic refrigeration

Magnetic refrigeration has been developed over many years by using the adiabatic demagnetization of electron spins in paramagnetic salt powders at the milliKelvin temperature range and nuclear spins in metals at the sub-milliKelvin temperature range [92]. As we show that paramagnetism can be induced in SiC by irradiation, Vlasov *et al.* proposed paramagnetic semiconductors, including SiC, as active media for refrigeration

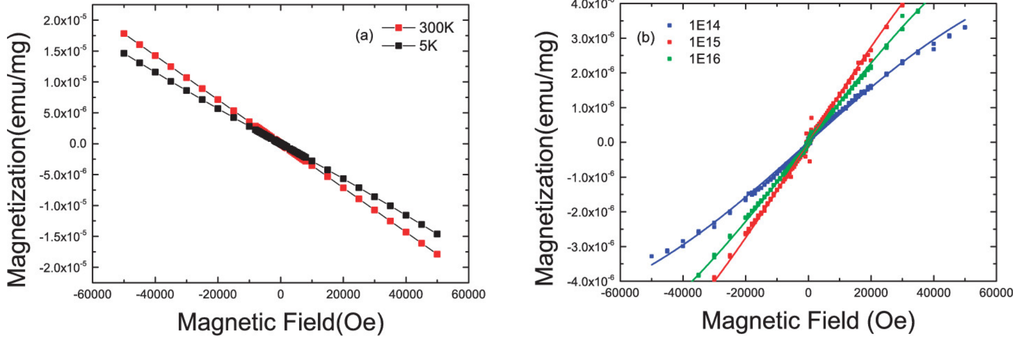

Figure 32. (a) M-H curves of the pristine 4H-SiC sample at 5 K and 300 K. (b) paramagnetic component of sample 1E14, 1E15 and 1E16 (the numbers are implantation fluence in cm^{-2}) at 5 K and the Brillouin fitting curve. The figures are from Ref. [91].

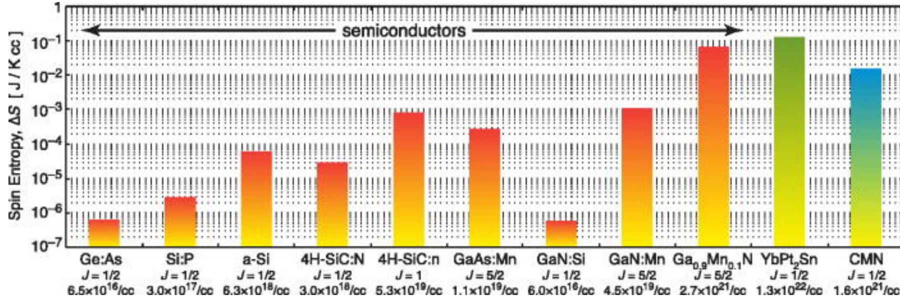

Figure 33. The theoretical spin entropy of different semiconductor systems. The values of the intermetallic compound $YbPt_2Sn_8$ and the commonly used paramagnetic salt CMN are shown as reference. The experimentally measured spin-J and spin density N_s are indicated for each system. The figure is from Ref. [93].

at cryogenic temperatures by adiabatic demagnetization [93]. Paramagnetism can come from un-ionized impurity dopants or structural defects, both contributing to local magnetic moments.

The specific spin entropy $\delta\zeta = k_B N_s ln(2J+1)$ available for magnetic refrigeration for SiC and other material systems, can be calculated by using the experimentally measured spin density N_s and angular momentum J. The results are shown in Fig. 33. It is shown that for doped semiconductors a large spin density is achievable in larger gap semiconductors (such as SiC). Neutron irradiation provides another method of introducing paramagnetism to semiconductors. A spin-1 density of N_s around 5.3×10^{19} cm^{-3} can be obtained in neutron irradiated 4H-SiC [52]. The simulated temperatures are shown in Fig. 34 for neutron irradiated 4H-SiC, Si:P, and GaN:Mn with particular spin and electron concentrations. The initial temperature was set equal to that of a reservoir at T_0 = 300 mK, and the zero-field time constant τ_0 = 3600 s represents a weak thermal link. The magnetic field profile was swept from an initial field B_i to a final field B_f at a constant sweep rate 100 mT/min. As shown by this simulation, it is possible to achieve a base temperature below 50 mK.

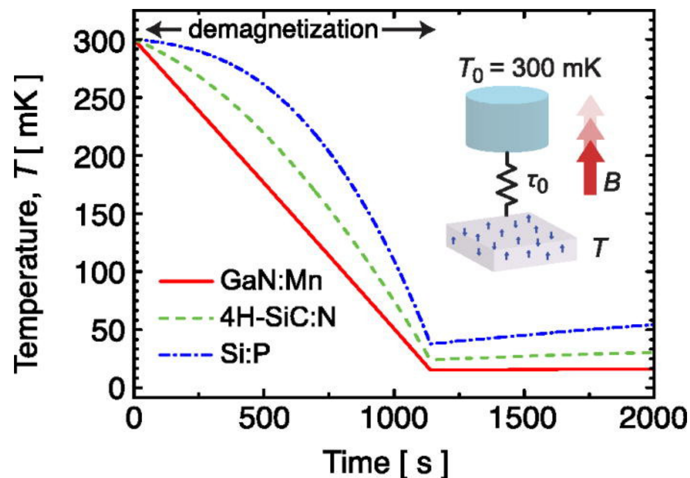

Figure 34. The simulated temperature T versus time t of Si:P, 4H-SiC:N and GaN:Mn with particular spin and electron concentrations, connected to a reservoir at $T_0 = 300\,\mathrm{mK}$ through a zero-field time constant of $\tau_0 = 3600\,\mathrm{s}$. The initial magnetic field of $\mathrm{B}_i = 2.0\,\mathrm{T}$ is swept to a final field of $\mathrm{B}_f = 0.1\,\mathrm{T}$ at a sweep rate of 100 mT/min. The figure is from Ref. [93].

The authors also pointed out that semiconductors, including SiC, are the most common substrate used for electronic and micro-electromechanical devices and thus offer the possibility of monolithic integration of solid state refrigerants with active devices [93].

4.4. Defects for quantum technology

The successful implementation of the nitrogen-vacancy (NV) center in diamond as a qubit has attracted a great deal of interest to utilize defects for quantum technology. In principle, similar defects can exist in other material systems. Indeed, in SiC silicon vacancy was found to combine the technological advantages of semiconductor quantum dots and the unique spin properties of the NV center in diamond [94]. Carbon antisite-vacancy pair in 4H-SiC created by electron irradiation and annealing was proposed to build room-temperature, photostable single-photon sources [95]. von Bardeleben *et al.* show that NV triplet centers can also be generated in all the main SiC polytypes as a platform for solid-state qubits and nanosensors [96]. Much different from diamond, SiC is already technologically and industrially relevant, due to its applications for high frequency and high power devices. Therefore, SiC offers a device-friendly platform for quantum technology. For details, we recommend a recent review paper by Ohshima *et al.* [97]

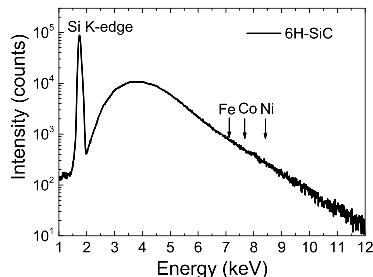

Figure 35. PIXE spectrum for the high-purity, semi-insulating 6H-SiC wafer by a broad proton beam. Within the detection limit, no Fe, Co or Ni contamination is observed. Figure is from Ref. [50].

5. Challenges

5.1. Contamination of transition metal impurities

Although defect induced magnetism has been reported in many material system, the measured magnetization remains as a weak signal slightly above the detection limit of sensitive SQUID magnetometry. On one hand, measurement artifacts in SQUID magnetometry may occur: improper mounting of samples and wrong use of sample holders can easily generate ferromagnetic like signal [98, 99]. On the other hand, there is always a debate over the purity of graphite and oxide substrates [100, 101]. Indeed, SiC has been developed to the microelectronic grade and contains much less impurities.

To check the trace presence of transition metals (Fe, Co and Ni, etc.) in high purity semi-insulating (HPSI) SiC substrates, particle-induced X-ray emission spectrometry (PIXE) presents a useful method with its bulk sensitivity of ppm amplitude without significant structural destruction [101]. One measurement for 6H-SiC is shown in Figure 35 by using 2 MeV protons with a broad beam of around 1 mm^2. In the spectrum, the sharp peak is the Si K-line X-ray emission. The broad bump is due to the secondary electron Bremsstrahlung background. For commercially available, purest graphite, there is detectable transition metal contamination (mainly Ti, V, Fe, Ni) as revealed by PIXE [101]. However, the transition metal impurity in the HPSI SiC, if there is, is below the detection limit of around 1 ppm (Fig. 35). Nevertheless, the sample purity should be carefully checked for studying defect induced magnetism.

On the other hand, the possible influence of low concentration impurities on the magnetism has been discussed in published papers. Shi *et al.* have grown undoped and V-doped 6H-SiC single crystals by the physical vapor transport method [102]. The V concentration is determined to be 3.76×10^{17} at./cm^3 and 6.14×10^{17} at./cm^3 by secondary ion mass spectrometry for low V-doped and high V-doped SiC samples, respectively. The undoped 6H-SiC shows only diamagnetism, but the V-doped 6H-SiC reveals ferromagnetism. The sample with lower V concentration shows stronger ferromagnetism compared to that of the sample with higher V concentration. It is

suggested that both V dopants and defects are essential for introducing ferromagnetism in V-doped SiC. In Ref. [103], the authors prepared Mn-doped 6H-SiC with Mn concentration below 10^{-3} molar fraction. The typical ferromagnetic order was established at as low Mn-doped concentration as 10^{-4} molar fraction at around 250 K. The authors speculated that the defect-related effects other than the Mn content play a more important role to determine the magnetic ordering. But the Mn impurities probably stabilize the wanted defects.

5.2. Spatial correlation between defects and magnetism

In many published results regarding defect induced magnetism, there are hints that the ferromagnetism is not homogenous. In Refs. [67, 52], the authors speculated that the ferromagnetic coupling can occur locally in some regions with proper defect concentration. For 3C-SiC, Liu *et al.* have disclosed that local magnetism is only on the (110) and (001) surfaces [104]. Esmaeily *et al.* have measured the magnetic properties of nanoporous alumina (Al_2O_3) membranes [105]. These membranes exhibit a temperature-independent and almost anhysteretic saturating response to a magnetic field up to temperatures of 300 K or higher. The magnetism increases with the area of the open nanopores. Crystallization of the membrane or treatment with salicylic acid can destroy 90% of the magnetism. The authors suggested that the effect is linked with the surfaces of the open pores in amorphous Al_2O_3.

Therefore, one needs an experiment which can measure the spatial distribution of ferromagnetism. Muon spin relaxation (μSR) measurements provide such a possibility. In μSR experiment, spin-polarized positive muons are implanted into materials. Each muon stopped in the lattice experiences the external and local magnetic fields and therefore precesses at a characteristic frequency. In experiment, the time evolution of the muon polarization P(t) is measured to get the information about the interaction of the muon magnetic moment with its magnetic environment. A single precession frequency is expected in a spatially homogenous ferromagnet or antiferromagnet. If the muons experience inhomogeneous magnetic fields, P(t) shows a distribution of precession frequencies (a "line shape") with the corresponding width. In a paramagnetic environment P(t) exhibits only slow exponential relaxation. Therefore, the local magnetic field distributions can be obtained on the atomic scale by μSR. The sensitivity allows the measurement of the internal magnetic fields below 0.1 Gauss in materials with very dilute magnetic moments [106, 107], ideally suitable for investigating defect induced magnetism.

μSR measurements was applied to investigate defect induced magnetism in ZnO [106, 107]. The magnetic volume is measured by the relaxing amplitude. For ZnO nanoparticles [106], the strongest relaxation is found for the fine grained sample, corresponding to a total magnetic volume fraction of about 35%. For the large grained sample, the magnetic volume fraction is approx. 15%. For ferromagnetic ZnO films, the volume fraction of the ferromagnetism phase is approximately 70%. Both researches

suggest that the defect induced ferromagnetism in ZnO is not homogenous. Similar experiments are expected for SiC.

5.3. Controlling charge states of defects

As we have discussed, the electronic structure of defects will depend on their charge states. However, it is challenging to manipulate the charge state in a controllable manner. In Ref. [77], the authors have suggested that nitrogen doping to substitute C atoms can manipulate the charge states of Si vacancy defects in 3C-SiC and the magnetic interactions between them [77]. We attempted to work on this issue by N and Al doping in 4H-SiC. The results show opposite behavior [78]. In Al-implanted SiC, relative strong ferromagnetism is observed. But in N-implanted SiC, the ferromagnetism is much weak. The reason is still unclear.

The charge states of both divacancy and Si vacancy have been demonstrated to be controllable by optical excitation with different wavelength [108, 109, 110]. For instance, under an excitation at energy levels below 1.3 eV, V_{Si}-V_C divacancies are switched from neutral to positively charged states [108]. This also gives perspective to control the defect induced magnetism in SiC by light.

6. Summary and outlook

Defect-induced ferromagnetism in ion implanted and neutron irradiated SiC has been observed by us and other groups. Some typical features describing conventional ferromagnetic materials are also observed in SiC, such as the magnetization dependence on the defect concentration, magnetic anisotropy, anomalous Hall effect (although very weak) and X-ray magnetic circular dichroism. These features in combination with first principles calculations demonstrate the intrinsic nature of the observed magnetism. However, there are still many questions unsolved. We list some of them as suggestions for future investigations.

(1) Locally identify the ferromagnetic regions or domains in SiC

From the investigations of ion implanted and neutron irradiated SiC, there is an accumulation of evidences that the ferromagnetic coupling is not homogenously occurring in the sample. The ferromagnetism distributes non-homogeneously in terms of its lateral distribution or depth distribution. Moreover, we are still uncertain if ferromagnetic domains with allowed orientations exist just like the normal ferromagnets. μSR measurements might be applied to confirm this speculation. A careful magnetic field microscopy investigation to scan over the surface is also a good means to this end. For the depth distribution, physical or chemical etching could be used to control the affected depth. Moreover, together with step by step magnetization measurement, one probably can identify the depth profile of the magnetization. Such an investigation may allow us to identify if the ferromagnetism is mainly at the surface, near some extended defects or depending on the irradiation depth.

Another possible method is nuclear probe ^{57}Fe. By implanting ^{57}Fe probe atoms, point defects and disorder will be created around these implanted probes and conversion electron Mössbauer spectroscopy can be performed on these probes. By measuring electric quadrupole and magnetic interactions simultaneously, magnetic properties will be obtained in the probe atomically local environment [111], providing us insight of defect induced magnetism in SiC at the atomic level.

(2) The magnetic state of a single defect in SiC

By scanning tunneling microscopy experiments, Ugeda *et al.* have observed a sharp electronic resonance at the Fermi energy around a single vacancy in graphite, which can be associated with the formation of local magnetic moment [63]. In the future, such an experiment for SiC should be feasible to clarify the magnetic state of a single defect. Scanning tunneling microscopy has been used to reveal the atomic structure at the surface of 6H-SiC [112].

(3) Thermal stability of defect-induced ferromagnetism in SiC

The thermal stability is the key factor for potential application because some defects will recombine or even disappear at room temperature. Sometimes the neutralization occurring at room temperature will also lead to the loss of the ferromagnetism. This is the major reason for the volatility for memory devices. Moreover, it will lead to a better understanding of the thermal dynamics of the defects especially in the paramagnetic regime. The annealing methods include a high temperature oven, rapid thermal annealing and sub-second annealing by flashlamps [113] and high power pulse Excimer laser. The aim is to confirm if the slightly damaged SiC can be completely recrystallized, i.e. recovered to the quality of the virgin SiC and to investigate the evolution of magnetic and optical properties at different annealing stages.

(4) The optical and electrical control of magnetism in SiC

One of the advantages of semiconductor materials exhibiting magnetism is the control of magnetism by optical and electrical methods without altering the semiconducting properties. Such a control has been demonstrated for GaMnAs by optical excitation and by electrical gating at low temperatures [114]. SiC with defect induced magnetism may provide such a test platform at room temperature.

7. Acknowledgments

The work was financially supported by the Helmholtz-Gemeinschaft Deutscher Forschungszentren (VH-NG-713) and by the Beijing Municipal Science and Technology Project (Grant Nos. Z171100002217004, D171100004517001, Z161100002116018). S. Z. thanks the ion implantation group at Ion Beam Center, HZDR. The authors are grateful to Manfred Helm for his critical reading of the manuscript.

8. References

[1] Stromberg F, Keune W, Chen X, Bedanta S, Reuther H and Mücklich A 2006 *J. Phys. Condens. Matter* **18** 9881

[2] Diallo M, Lechevallier L, Fnidiki A, Lardé R, Debelle A, Thomé L, Viret M, Marteau M, Eyidi D, Declémy A *et al.* 2015 *J. Appl. Phys.* **117** 183907

[3] Dietl T 2002 *Semicond. Sci. Technol.* **17** 377

[4] Esquinazi P, Spemann D, Höhne R, Setzer A, Han K H and Butz T 2003 *Phys. Rev. Lett.* **91** 227201

[5] Xia H, Li W, Song Y, Yang X, Liu X, Zhao M, Xia Y, Song C, Wang T W, Zhu D *et al.* 2008 *Adv. Mater.* **20** 4679–4683

[6] Yang X, Xia H, Qin X, Li W, Dai Y, Liu X, Zhao M, Xia Y, Yan S and Wang B 2009 *Carbon* **47** 1399–1406

[7] Coey J M D, Stamenov P, Gunning R, Venkatesan M and Paul K 2010 *New J. Phys.* **12** 053025

[8] Song B, Bao H, Li H, Lei M, Peng T, Jian J, Liu J, Wang W, Wang W and Chen X 2009 *J. Am. Chem. Soc.* **131** 1376–1377

[9] Yi J, Lim C, Xing G, Fan H, Van L, Huang S, Yang K, Huang X, Qin X, Wang B *et al.* 2010 *Phys. Rev. Lett.* **104** 137201

[10] Sundaresan A, Bhargavi R, Rangarajan N, Siddesh U and Rao C N R 2006 *Phys. Rev. B* **74** 161306

[11] Garcia M, Merino J, Fernández Pinel E, Quesada A, De la Venta J, Ruíz González M, Castro G, Crespo P, Llopis J, González-Calbet J *et al.* 2007 *Nano Lett.* **7** 1489–1494

[12] Volnianska O and Boguslawski P 2010 *J. Phys. Condens. Matter* **22** 073202

[13] Esquinazi P, Hergert W, Spemann D, Setzer A and Ernst A 2013 *IEEE Trans. Magn.* **49** 4668–4674

[14] Zhou S 2014 *Nucl. Instrum. Methods. Phys. Res. B* **326** 55–60

[15] Kimoto T 2015 *Jpn. J. Appl. Phys.* **54** 040103

[16] Ramsdell L S 1947 *Am. Mineral.* **32** 64–82

[17] Casady J and Johnson R W 1996 *Solid State Electron.* **39** 1409–1422

[18] Powell A R and Rowland L B 2002 *Proc. IEEE* **90** 942–955

[19] Torpo L, Marlo M, Staab T and Nieminen R 2001 *J. Phys. Condens. Matter* **13** 6203

[20] Weber J, Koehl W, Varley J, Janotti A, Buckley B, Van de Walle C and Awschalom D 2011 *J. Appl. Phys.* **109** 102417

[21] Bechstedt F, Fissel A, Furthmüller J, Grossner U and Zywietz A 2001 *J. Phys. Condens. Matter* **13** 9027

[22] Kimoto T, Nakazawa S, Hashimoto K and Matsunami H 2001 *Appl. Phys. Lett.* **79** 2761–2763

[23] Fujihira K, Kimoto T and Matsunami H 2002 *Appl. Phys. Lett.* **80** 1586–1588

[24] Zhang J, Storasta L, Bergman J, Son N and Janzén E 2003 *J. Appl. Phys.* **93** 4708–4714

[25] Ziegler J F, Ziegler M and Biersack J 2010 *Nucl. Instrum. Methods. Phys. Res. B* **268** 1818 – 1823 19th International Conference on Ion Beam Analysis

[26] Devanathan R and Weber W J 2000 *J. Nucl. Mater.* **278** 258–265

[27] Krasheninnikov A and Nordlund K 2010 *J. Appl. Phys.* **107** 3

[28] Storasta L, Bergman J, Janzén E, Henry A and Lu J 2004 *J. Appl. Phys.* **96** 4909–4915

[29] Chen X D, Yang C L, Gong M, Ge W K, Fung S, Beling C D, Wang J N, Lui M K and Ling C C 2004 *Phys. Rev. Lett.* **92**(12) 125504

[30] Wendler E, Bierschenk T, Felgenträger F, Sommerfeld J, Wesch W, Alber D, Bukalis G, Prinsloo L C, van der Berg N, Friedland E *et al.* 2012 *Nucl. Instr. Meth. Phys. Res. B* **286** 97–101

[31] Kelly B, Marsden B, Hall K, Martin D, Harper A and Blanchard A 2000 *IAEA Tecdoc* **1154**

[32] Cartz L, Karioris F, Roult G and Labbe J 1984 *Radiation Effects* **85** 57–59

[33] Zvanut M E 2004 *J. Phys. Condens. Matter* **16** R1341

[34] Isoya J, Umeda T, Mizuochi N, Son N, Janzén E and Ohshima T 2008 *Phys. Status Solidi B* **245** 1298–1314

[35] Son N, Hai P, Wagner M, Chen W, Ellison A, Hallin C, Monemar B and Janzén E 1999 *Semicond. Sci. Technol.* **14** 1141

[36] Gordon L, Janotti A and Van de Walle C G 2015 *Phys. Rev. B* **92** 045208

[37] Koehl W F, Buckley B B, Heremans F J, Calusine G and Awschalom D D 2011 *Nature* **479** 84
[38] Pensl G and Choyke W J 1993 *Physica B* **185** 264–283
[39] Hemmingsson C, Son N T, Kordina O, Bergman J, Janzén E, Lindström J, Savage S and Nordell N 1997 *J. Appl. Phys.* **81** 6155–6159
[40] David M, Alfieri G, Monakhov E, Hallén A, Blanchard C, Svensson B and Barbot J 2004 *J. Appl. Phys.* **95** 4728–4733
[41] Ayedh H, Nipoti R, Hallén A and Svensson B 2015 *Appl. Phys. Lett.* **107** 252102
[42] Ahmed E M H 2008 *Characterization of Control Mesoporous Glasses (CPGs) Using Positron Annihilation Lifetime Spectroscopy (PALS)* Ph.D. thesis Martin Luther University Halle-Wittenberg
[43] Rempel A and Schaefer H E 1995 *Appl. Phys. A* **61** 51–53
[44] Ling C, Deng A, Fung S and Beling C 2000 *Appl. Phys. A* **70** 33–38
[45] Ling C, Beling C and Fung S 2000 *Phys. Rev. B* **62** 8016
[46] Brauer G, Anwand W, Coleman P, Störmer J, Plazaola F, Campillo J, Pacaud Y and Skorupa W 1998 *J. Phys. Condens. Matter* **10** 1147
[47] Brauer G, Anwand W, Coleman P, Knights A, Plazaola F, Pacaud Y, Skorupa W, Störmer J and Willutzki P 1996 *Phys. Rev. B* **54** 3084
[48] Liu Y, Wang G, Wang S, Yang J, Chen L, Qin X, Song B, Wang B and Chen X 2011 *Phys. Rev. Lett.* **106**(8) 087205
[49] Anwand W, Brauer G and Skorupa W 2002 *Appl. Surf. Sci.* **194** 131 – 135
[50] Wang Y, Liu Y, Wang G, Anwand W, Jenkins C A, Arenholz E, Munnik F, Gordan O D, Salvan G, Zahn D R *et al.* 2015 *Sci. Rep.* **5** 8999
[51] Yu L, Jin H, Liu D, Dai Y, Guo M, Huang B and Zhang Z 2010 *Chem. Phys. Lett.* **496** 276 – 279
[52] Wang Y, Liu Y, Wendler E, Hübner R, Anwand W, Wang G, Chen X, Tong W, Yang Z, Munnik F *et al.* 2015 *Phys. Rev. B* **92** 174409
[53] Li L, Prucnal S, Yao S D, Potzger K, Anwand W, Wagner A and Zhou S 2011 *Appl. Phys. Lett.* **98** 222508
[54] Weber W, Wang L, Yu N and Hess N 1998 *Mater. Sci. & Eng. A* **253** 62 – 70
[55] Wang Y, Chen X, Li L, Shalimov A, Tong W, Prucnal S, Munnik F, Yang Z, Skorupa W, Helm M and Zhou S 2014 *J. Appl. Phys.* **115** 17C104
[56] Li L, Hua W, Prucnal S, Yao S D, Shao L, Potzger K and Zhou S 2012 *Nucl. Instrum. Methods Phys. Res. B* **275** 33 – 36
[57] Zheng H, Yan Y, Lv Z, Yang S, Li X, Liu J, Ye B, Peng C, Diao C and Zhang W 2013 *Appl. Phys. Lett.* **102** 142409
[58] He X, Tan J, Zhang B, Zhao M, Xia H, Liu X, He Z, Yang X and Zhou X 2013 *Appl. Phys. Lett.* **103** 262409
[59] Lv Z, Ma X, Zheng H, An R, Peng C, Liu J, Ye B, Diao C, Liu X and Zhang W 2013 *Mater. Lett.* **93** 374 – 376
[60] Zhou R W, Liu X C, Wang H J, Chen W B, Li F, Zhuo S Y and Shi E W 2015 *AIP Advances* **5** 047146
[61] Li Q, Xu J, Liu J and Ye B 2016 *Mater. Res. Exp.* **3** 056103
[62] Lehtinen P O, Foster A S, Ma Y, Krasheninnikov A V and Nieminen R M 2004 *Phys. Rev. Lett.* **93**(18) 187202
[63] Ugeda M M, Brihuega I, Guinea F and Gómez-Rodríguez J M 2010 *Phys. Rev. Lett.* **104** 096804
[64] Yazyev O V 2010 *Rep. Prog. Phys.* **73** 056501
[65] Wang Y, Pochet P, Jenkins C A, Arenholz E, Bukalis G, Gemming S, Helm M and Zhou S 2014 *Phys. Rev. B* **90** 214435
[66] Semenov A, Pashchenko V, Khirnyi V, Kozlovskyi and Mateichenko P 2015 *Physica E* **74** 220 – 225
[67] Wang Y, Li L, Prucnal S, Chen X, Tong W, Yang Z, Munnik F, Potzger K, Skorupa W, Gemming S *et al.* 2014 *Phys. Rev. B* **89** 014417

[68] Bean C P and Livingston J D 1959 *J. Appl. Phys.* **30**
[69] Shiratsuchi Y, Endo Y and Yamamoto M 2004 *Thin Solid Films* **464-465** 141 – 145
[70] Zhou S, Potzger K, Xu Q, Kuepper K, Talut G, Markó D, Mücklich A, Helm M, Fassbender J, Arenholz E and Schmidt H 2009 *Phys. Rev. B* **80**(9) 094409
[71] Slawska-Waniewska A, Gutowski M, Lachowicz H K, Kulik T and Matyja H 1992 *Phys. Rev. B* **46**(22) 14594
[72] Jamet M, Barski A, Devillers T, Poydenot V, Dujardin R, Bayle-Guillemaud P, Rothman J, Bellet-Amalric E, Marty A, Cibert J, Mattana R and Tatarenko S 2006 *Nature Mater.* **5** 653–659
[73] Thiess A, Dederichs P H, Zeller R, Blügel S and Lambrecht W R L 2012 *Phys. Rev. B* **86**(18) 180401
[74] Qin S, Guo X, Cao Y, Ni Z and Xu Q 2014 *Carbon* **78** 559 – 565
[75] Barzola-Quiquia J, Esquinazi P, Rothermel M, Spemann D, Butz T and García N 2007 *Phys. Rev. B* **76**(16) 161403
[76] Ramos M A, Barzola-Quiquia J, Esquinazi P, Muñoz Martin A, Climent-Font A and Garcia-Hernandez M 2010 *Phys. Rev. B* **81**(21) 214404
[77] Zhao M, Pan F and Mei L 2010 *Appl. Phys. Lett.* **96** 012508
[78] Liu Y, Yuan Y, Liu F, Böttger R, Anwand W, Wang Y, Semisalova A, Ponomaryov A N, Lu X, Arenholz E *et al.* 2017 *Phys. Rev. B* **95** 195309
[79] Morbec J M and Rahman G 2013 *Phys. Rev. B* **87** 115428
[80] Stohr J, Padmore H, Anders S, Stammler T and Scheinfein M 1998 *Surf. Rev. Lett.* **5** 1297–1308
[81] Ney A, Opel M, Kaspar T C, Ney V, Ye S, Ollefs K, Kammermeier T, Bauer S, Nielsen K, Goennenwein S *et al.* 2010 *New J. Phys.* **12** 013020
[82] Ohldag H, Esquinazi P, Arenholz E, Spemann D, Rothermel M, Setzer A and Butz T 2010 *New J. Phys.* **12** 123012
[83] Gao X, Chen S, Liu T, Chen W, Wee A, Nomoto T, Yagi S, Soda K and Yuhara J 2008 *Phys. Rev. B* **78** 201404
[84] Dedkov Y S and Fonin M 2010 *New J. Phys.* **12**
[85] He M, He X, Lin L, Song B and Zhang Z 2014 *Solid State Commun.* **197** 44 – 48
[86] Zhang Z T, Dmytriieva D, Molatta S, Wosnitza J, Wang Y, Helm M, Zhou S and Kühne H 2017 *Phys. Rev. B* **95**(8) 085203
[87] Jiang W, Zhang Y and Weber W J 2004 *Phys. Rev. B* **70** 165208
[88] Debelle A, Thomé L, Dompoint D, Boulle A, Garrido F, Jagielski J and Chaussende D 2010 *J. Phys. D: Appl. Phys.* **43** 455408
[89] Malherbe J B 2013 *J. Phys. D: Appl. Phys.* **46** 473001
[90] Heera V, Prokert F, Schell N, Seifarth H, Fukarek W, Voelskow M and Skorupa W 1997 *Appl. Phys. Lett.* **70** 3531–3533
[91] Peng B, Jia R X, Wang Y T, Dong L P, Hu J C and Zhang Y M 2016 *AIP Advances* **6** 095201
[92] Pobell F 1996 *Matter and Methods at Low Temperatures* vol 2 (Springer)
[93] Vlasov A, Guillemette J, Gervais G and Szkopek T 2017 *Appl. Phys. Lett.* **111** 142102
[94] Riedel D, Fuchs F, Kraus H, Väth S, Sperlich A, Dyakonov V, Soltamova A, Baranov P, Ilyin V and Astakhov G 2012 *Phys. Rev. Lett.* **109** 226402
[95] Castelletto S, Johnson B, Ivády V, Stavrias N, Umeda T, Gali A and Ohshima T 2014 *Nature materials* **13** 151
[96] Von Bardeleben H, Cantin J, Csóré A, Gali A, Rauls E and Gerstmann U 2016 *Phys. Rev. B* **94** 121202
[97] Ohshima T, Satoh T, Kraus H, Astakhov G V, Dyakonov V and Baranov P G 2018 *J. Phys. D: Appl. Phys.* **51** 333002
[98] Sawicki M, Stefanowicz W and Ney A 2011 *Semicond. Sci. Technol.* **26** 064006
[99] Pereira L, Araújo J, Van Bael M, Temst K and Vantomme A 2011 *J. Phys. D: Appl. Phys.* **44** 215001

[100] Sepioni M, Nair R R, Tsai I L, Geim A K and Grigorieva I V 2012 *EPL (Europhysics Letters)* **97** 47001

[101] Spemann D, Esquinazi P, Setzer A and Böhlmann W 2014 *AIP Adv.* **4** 107142

[102] Shi-Yi Z, Xue-Chao L, Ze X, Wen-Sheng Y, Jun X, Jian-Hua Y and Er-Wei S 2012 *Chin. Phys. B* **21** 067503

[103] Song B, Bao H, Li H, Lei M, Jian J, Han J, Zhang X, Meng S, Wang W and Chen X 2009 *Appl. Phys. Lett.* **94** 102508

[104] Liu L Z, Wu X L, Liu X X, Xiong S J and Chu P K 2014 *J. Phys. Chem. C* **118** 25429–25433

[105] Esmaeily A S, Venkatesan M, Sen S and Coey J 2018 *Phys. Rev. Mater.* **2** 054405

[106] Tietze T, Audehm P, Chen Y C, Schütz G, Straumal B B, Protasova S G, Mazilkin A A, Straumal P B, Prokscha T, Luetkens H *et al.* 2015 *Sci. Rep.* **5** 8871

[107] Tseng L, Suter A, Wang Y, Xiang F, Bian P, Ding X, Tseng A, Hu H, Fan H, Zheng R *et al.* 2017 *Phys. Rev. B* **96** 104423

[108] Golter D and Lai C 2017 *Sci. Rep.* **7** 13406

[109] Wolfowicz G, Anderson C P, Yeats A L, Whiteley S J, Niklas J, Poluektov O G, Heremans F J and Awschalom D D 2017 *Nature Communications* **8** 1876

[110] Magnusson B, Son N T, Csóré A, Gällström A, Ohshima T, Gali A and Ivanov I G 2018 *Phys. Rev. B* **98**(19) 195202

[111] Sielemann R, Kobayashi Y, Yoshida Y, Gunnlaugsson H P and Weyer G 2008 *Phys. Rev. Lett.* **101**(13) 137206

[112] Li L and Tsong I 1996 *Surf. Sci.* **351** 141 – 148

[113] Rebohle L, Prucnal S and Skorupa W 2016 *Semicond. Sci. Technol.* **31** 103001

[114] Nazmul A M, Kobayashi S, Sugahara S and Tanaka M 2004 *J. J. Appl. Phys.* **43** L233